Research Square

Preprints are preliminary reports that have not undergone peer review.
They should not be considered conclusive, used to inform clinical practice,
or referenced by the media as validated information.

Investigation of Photocatalytic, Piezoelectric and Dielectric Properties of Sol- Gel Synthesized Barium Titanate Nanoparticles Reinforced into PMMA Polymer Matrices Nanocomposites for Multifunctional Applications

Md. Tanzim Shahriar

2013005@student.ruet.ac.bd

Rajshahi University of Engineering and Technology

Abdullah Wasif Rafin

Rajshahi University of Engineering and Technology

Foysal Anwar

Rajshahi University of Engineering and Technology

Mohammad Shahed Hasan Khan Tushar

Rajshahi University of Engineering and Technology

Suravi Islam

Aminur Rahman

Research Article

Keywords: Barium Titanate, PMMA, Nanocomposite, Dielectric, Piezoelectric, Photocatalytic

Posted Date: November 10th, 2026

DOI: https://doi.org/10.21203/rs.3.rs-11053564/v1

License: This work is licensed under a Creative Commons Attribution 4.0 International License.
Read Full License

Additional Declarations: No competing interests reported.

Investigation of Photocatalytic, Piezoelectric and Dielectric Properties of Sol-Gel Synthesized Barium Titanate Nanoparticles Reinforced into PMMA Polymer Matrices Nanocomposites for Multifunctional Applications

Md. Tanzim Shahriar[1(a)*], Abdullah Wasif Rafin[1(b)*], Foysal Anwar[1(c)], Mohammad Shahed Hasan Khan Tushar[1(d)], Suravi Islam[2], Aminur Rahman[3]

[1(a), (b), (c)] Department of Materials Science & Engineering, Rajshahi University of Engineering & Technology,
Bangladesh.
[1(d)]Department of Mechanical Engineering, Rajshahi University of Engineering & Technology,
Bangladesh.
[2]Institute of Glass and Ceramic Research and Testing (IGCRT), BCSIR, Dhaka-1205, Bangladesh.
[3]The Institute of Mining, Mineralogy and Metallurgy (IMMM), BCSIR, Joypurhat-5900, Bangladesh.

[1(a)*]Email: 2013005@student.ruet.ac.bd; [1(b)*]Email:1913057@student.ruet.ac.bd ; [1(c)]Email: foysalanwarfaf@gmail.com [1(d)]Email: mstushar@me.ruet.ac.bd

ABSTRACT

This research focuses on the synthesis and characterization of nanocomposites consisting of barium titanate ($BaTiO_3$) nanoparticles reinforced into poly(methyl methacrylate) (PMMA) polymer matrices. The nanocomposites were prepared using a solution-casting technique, while the barium titanate nanoparticles were synthesized via a conventional sol-gel method followed by calcination at 800°C for 1 hour. Structural, morphological, photocatalytic, piezoelectric, and dielectric properties were evaluated using several characterization techniques, including FTIR, XRD, SEM, UV-Vis spectroscopy, a d33 meter, and an LCR analyzer. FTIR analysis identified absorption bands corresponding to Ba-O and Ti-O, as well as organic functional groups associated with the PMMA polymer matrices. XRD analysis confirmed the tetragonal structure of $BaTiO_3$ nanoparticles with an average crystallite size of 14.49 nm. SEM analysis determined the particle size to be approximately 37 nm. UV-Vis spectroscopy evaluated the nanoparticles band-gap 2.92 eV and assessed photocatalytic activity. Under UV irradiation, both nanocomposites progressively degraded methylene blue (MB), with the 30 wt% BTO/PMMA nanocomposite achieving the highest degradation efficiency of 24.41% after 75 min. The piezoelectric co-efficient was evaluated 35 pC/N and 37 pC/N with d_{33} meter analysis. The dielectric, impedance and modulus characteristics were observed over the low-high frequency range 40-110 MHz. The dielectric constant was determined 4.35 and 17.11 for 20 and 30 wt% BTO/PMMA nanocomposites, respectively, at low frequency range, which decreased gradually with increasing frequency, following modest dielectric constant 3.36 and 9.98 at high frequency range 1M-110M Hz, along with high ac conductivity 3.5×10^{-3} Scm^{-1} and 5.98×10^{-3} Scm^{-1}. Impedance and electrical-

modulus analysis further revealed broad non-Debye relaxation behavior associated with heterogeneous BTO/PMMA interfaces and localized charge-transport processes. The dispersion of Z″ and M″ plots with increasing frequency indicates the occurrence of dielectric relaxation. Overall, these results identified relatively higher $BaTiO_3$ reinforcement enhanced multifunctional properties which support BTO/PMMA nanocomposite as a promising processable platform for dielectric components and photocatalytic pollutant-remediation applications.

Key Words: Barium Titanate, PMMA, Nanocomposite, Dielectric, Piezoelectric, Photocatalytic

1. INTRODUCTION

The rapid development of miniaturized electronics, distributed sensing technologies, and advanced environmental remediation systems has intensified the demand for materials capable of delivering multiple functions within compact, processable architectures. Conventional dielectric, electromechanical, and photocatalytic technologies commonly rely on distinct classes of functional materials, increasing fabrication complexity and limiting their inclusion in multifunctional platforms [1]. Polymer–ceramic nanocomposites provide a beneficial route to overcome this drawback by combining the low density, electrical insulation, mechanical compliance, and processability of polymers with the high electric polarizability and functional responses of electroactive ceramics [2], [3]. Such integrated systems are particularly attractive because dielectric polarization, piezoelectric mechanical-to-electrical conversion, and photocatalytic photoinduced activity can be combined within a single processable material platform [2], [4].

Among lead-free functional ceramics, barium titanate ($BaTiO_3$, BTO) is attractive because of its high dielectric permittivity, ferroelectric polarization, and well-established piezoelectric response [5], [6]. These properties have enabled its use in capacitive components, sensors, actuators, and electromechanical energy-conversion systems. $BaTiO_3$ can also exhibit semiconductor-mediated photocatalytic activity under adequate irradiation, where excitation across the band gap generates electron–hole pairs, which participate in surface redox reactions and facilitate the formation of reactive oxygen species [7], [8]. This photoactivity has extended $BaTiO_3$-based materials toward degrading persistent organic contaminants, including methylene blue [7], [8]. Despite this adaptability, direct use of BTO has important functional restrictions. Bulk $BaTiO_3$ ceramics are rigid, brittle, and typically require high-temperature processing [9]. In contrast, nanoscale $BaTiO_3$ particles exhibit a strong tendency to agglomerate, which complicates their fabrication into continuous and mechanically robust structures [10]. These limitations motivate combining $BaTiO_3$ with a suitable polymeric matrix.

Reinforcing $BaTiO_3$ within poly(methyl methacrylate) (PMMA) provides a rational strategy for retaining the functional characteristics of the ceramic while overcoming these processing and mechanical restrictions. PMMA offers low density, mechanical stability, optical transparency, and

compatibility with solution-based fabrication. Although PMMA possesses relatively low dielectric permittivity and modest intrinsic electromechanical functionality, it provides a suitable and processable matrix for functional enhancement through ceramic reinforcement [11]. $BaTiO_3$ and PMMA therefore form a complementary architecture: the ceramic phase contributes strong polarization, piezoelectric activity, and photoactive sites, whereas PMMA provides structural continuity, processability, mechanical support, and immobilization of the nanoparticles [6], [7], [8], [11], [12]. Previous studies have demonstrated that incorporating $BaTiO_3$ into PMMA can enhance dielectric performance while preserving important polymer attributes [5], [13], [14], [15]. Earlier work emphasized that homogeneous BTO distribution is vital for reliable dielectric behavior [15]. Another study demonstrated that improved ceramic–polymer compatibility can suppress nanoparticle aggregation while maintaining the flexibility and workability of BTO/PMMA nanocomposites [5].

The multifunctional response of BTO/PMMA nanocomposites depends on the intrinsic properties of the constituent phases, ceramic-particle dispersion, and the characteristics of the ceramic–polymer interface. A higher $BaTiO_3$ content increases the amount of highly polarizable material and the density of heterogeneous interfaces, which can enhance interfacial or Maxwell–Wagner–Sillars polarization. In contrast, reduced interparticle separation and agglomeration can intensify local electric-field distortion, interfacial charge accumulation, dielectric loss, and nonuniform charge transport [16], [17], [18]. These microstructural factors also influence electromechanical performance because the effective utilization of $BaTiO_3$ piezoelectricity depends on the active ceramic fraction, particle connectivity, interfacial adhesion, and mechanical stress transfer through the polymer matrix [9], [19], [20]. Furthermore, $BaTiO_3$ introduces a photoactive pathway under UV irradiation, in which photogenerated electrons and holes initiate surface reactions that generate reactive species capable of degrading organic dye molecules [7], [8]. Within the composite, PMMA primarily provides structural support and immobilization, while dispersed $BaTiO_3$ serves as photoactive ceramic sites. Therefore, particle accessibility, dispersion, and polymer–ceramic interactions significantly influence the photocatalytic response [19], [21]. Ceramic reinforcement and interfacial structure thus represent common design parameters that link the dielectric, piezoelectric, and photocatalytic responses of BTO/PMMA nanocomposites. However, their combined dependence on $BaTiO_3$ concentration and ceramic–polymer interfaces remains underexplored [5], [13], [14], [15], [19], [21], [22].

This study focuses on developing BTO/PMMA nanocomposites containing comparatively modest $BaTiO_3$ reinforcement of 20 wt% and 30 wt% and systematically evaluating their structural, morphological, dielectric, piezoelectric, and photocatalytic properties through FTIR, XRD, SEM, LCR meter, d_{33} meter and UV-Vis analyzer, respectively. $BaTiO_3$ nanoparticles were synthesized via a sol–gel-assisted route and incorporated into PMMA by solution casting. Together, these synthesis and analysis clarified how $BaTiO_3$ reinforcement and ceramic–polymer interfaces govern multifunctional performance, thereby addressing the gap between predominantly single-function BTO/polymer studies and multifunctional composite design. The resulting structure–property

relationships provide a basis for considering BTO/PMMA nanocomposites as a processable multifunctional platform for dielectric and capacitive components, piezoelectric sensing and mechanical-energy transduction, and photoactive pollutant-remediation systems.

2. MATERIALS & METHODOLOGY

2.1. Materials

High-purity barium acetate [$Ba(CH_3COO)_2$, ≥99.5%; Researchlab Fine Chem Industries, Mumbai, India] and titanium(IV) isopropoxide [$Ti(OCH(CH_3)_2)_4$, ≥99.5%; Researchlab Fine Chem Industries, Mumbai, India] were utilized as the barium and titanium precursors, respectively. 2-Propanol [CH3CH(OH)CH3; Merck KGaA 64271 Darmstadt, Germany] was used as the reaction medium. Poly(methyl methacrylate) (PMMA) pellets, dimethyl sulfoxide (DMSO) [$C_2H_6OS\{CH_3\}_2SO$, Merck KGaA 64271 Darmstadt, Germany], and acetone [(CH3COCH3); Merck KGaA 64271 Darmstadt, Germany] served as the polymer matrix and co-solvents during nanocomposite fabrication. All reagents were used as received without further purification.

2.2. Synthesis of Nanoparticles:

$BaTiO_3$ (BTO) nanoparticles were synthesized via conventional soi-gel procedure. The starting materials for this synthesis used Barium Acetate [Ba $(CH_3COO)_2$], Titanium (IV) Isopropoxide

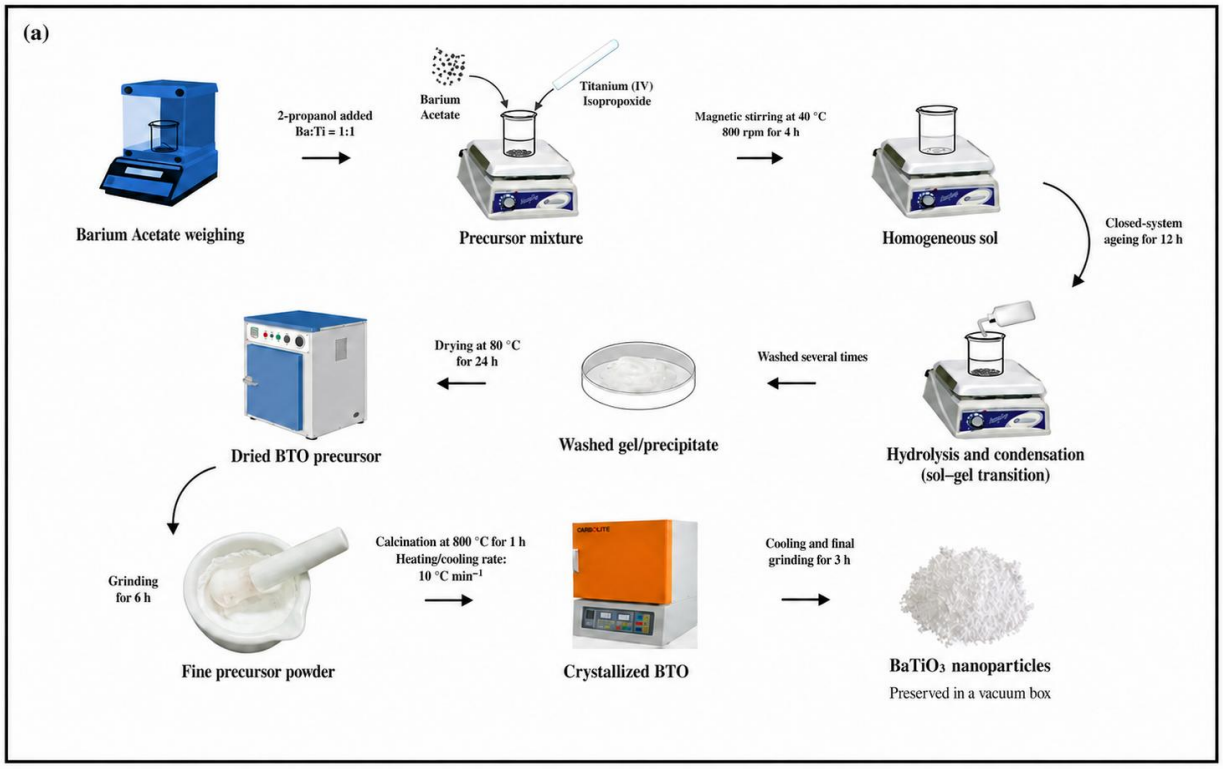


Figure 2.1. Schematic illustration of the sol-gel synthesis of $BaTiO_3$ nanoparticles

$Ti[OCH(CH_3)_2]_4$, where 19 cc of titanium isopropoxide and 16.4g of barium acetate were measured as a Ba:Ti molar ratio 1:1 and made a clear solution within a 2-propanol solvent. Approximately 50ml 2-propanol solvent were added. One beaker containing the solvent was gradually filled with the weighed amounts of barium acetate and titanium isopropoxide. The mixture was stirred with a magnetic stirrer at 800 rpm with 40°C for 4 hours until the barium acetate was completely dissolved. Then the solution was kept in a closed system for 12 hours. Following complete mixing of the precursor solutions, hydrolysis and condensation processes led to the sol-gel transition. Then the solution was washed several times to reduce contaminates then dried for 24 hours at 80°C. The organic species and solvent were eliminated during this phase, leaving only the precursor oxide powder. Subsequently, the dried powder was ground in mortar pastel at least for 6 hours. Then a heating rate of 10°C/min was applied to heating the samples from room temperature to a maximum temperature of 800°C for calcination, followed by holding at 800°C for 1 hour in a furnace and then cooled down to room temperature with a cooling rate of 10°C/min with required times. Then the calcined powder was further ground in mortar-pastel for additional 3 hours. After 10 minutes of grinding the sample was dried for 10 minutes at 100°C in oven. The calcined nanoparticles in powder form were preserved in vacuum box for characterizations.

2.3. Synthesis of BTO/PMMA Nanocomposite:

The BTO/PMMA solution were created with great care using a precise solvent casting technique. The first phase was submitting polymers pellets to a comprehensive drying procedure using a vacuum oven, wherein a temperature of 90°C was maintained for a period of 24 hours. The implementation of this crucial pre-processing step facilitated the elimination of any remaining moisture, ensuring the integrity of the polymer blend. After the completion of the drying procedure, a composition consisting of PMMA was measured. The addition of a combination consisting of dimethyl sulfoxide (DMSO) and acetone, with a volumetric ratio of 30:70, was performed in order to achieve a uniform blend. This mixture was added to the 5g weighted PMMA. Following this, the composite underwent vigorous stirring on a heated plate for a duration of 3 hours, facilitating the dissolution of the polymers in the solvent combination. In order to include the synthesized BTO nanoparticles into polymer matrices, same ratios of 20% were introduced into the respective beakers. The remaining weight percentage consisted of the solvents dimethyl sulfoxide (DMSO) and acetone, which were essential for preserving the intended viscosity. The uniformity of the mixture and dispersion of particles were facilitated with a 30- minute sonication procedure using an ultrasound sonicate machine, operating at of 30°C. Then, BTO nanoparticles were added at 30% ratio and the mixes underwent continuous agitation at a temperature of 80°C for a prolonged period of 2 hours following 3 times the same process, utilizing a stirring speed of 1500 rpm. The extended duration of mixing facilitated the homogeneous dispersion of BTO particles within the PMMA matrices. After attaining the appropriate degree of uniformity and coherence, the amalgamation was cautiously transferred into a petri-dish and afterwards introduced into an oven. The petri- dish was subjected to a curing period of 48 hours, during which it was exposed to a constant temperature

of 60°C. Thus, the successful synthesis of BTO/PMMA nanocomposites were achieved by the implementation of a complete method.

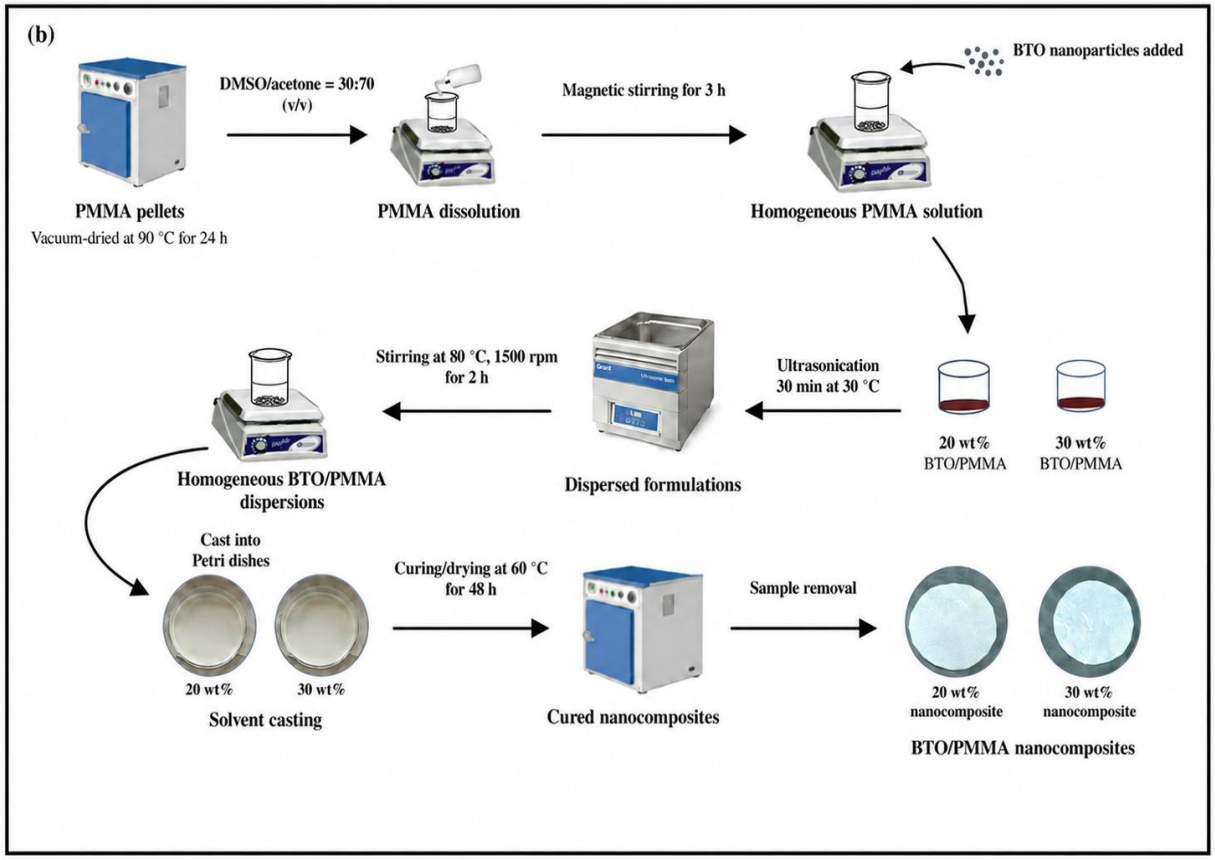


Figure 2.2. Schematic illustration of BTO/PMMA nanocomposite fabrication

3. RESULT & DISCUSSION

3.1. Structural Analysis

3.1.1. Fourier Transform Infrared Spectroscopy (FTIR) Analysis

The FTIR spectrum of $BaTiO_3$ nanoparticles showed well defined peaks located at 526 cm^{-1} for Ti-O stretching of TiO_6 octahedral sites and 856 cm^{-1} for Ti-O-Ti bridging vibration, associated with Ti-O network, in Figure. 3.1 [23], [24]. Besides, The CO_3^{2-} asymmetric stretching indicated a prominent peak at 1430 cm^{-1}. The O-H stretching band was attributed at 3776 cm^{-1}, usually associated with surface adsorbed hydroxyl groups from moisture. Figure 3.2 showed the FTIR spectra for 20 wt% and 30 wt% BTO/PMMA nanocomposites. Both spectra exhibit characteristic PMMA vibrational bands and a low-wavenumber metal–oxygen absorption band attributed to $BaTiO_3$, indicating the successful incorporation of BTO nanoparticles into the PMMA matrix [23].

Previous studies on similar $BaTiO_3$/PMMA systems have reported Ti–O vibrations in the low-wavenumber region and ester-related C–O stretching bands from the PMMA phase [14], [25].

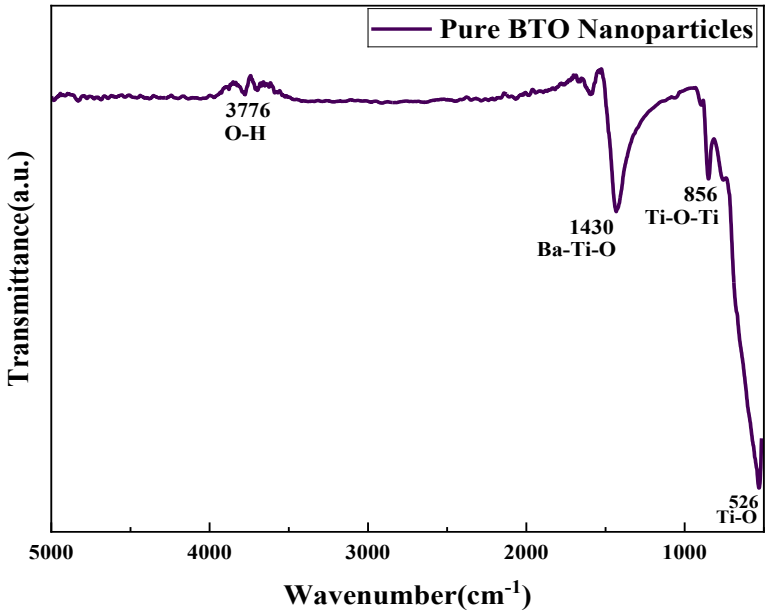


Figure 3.1. FTIR graph of pure $BaTiO_3$ nanoparticles after calcination.

The absorption band was observed in both nanocomposites for Ti–O stretching at 505 cm^{-1} within the TiO_6 octahedra of the $BaTiO_3$ perovskite lattice. The persistence of this band indicated that the $BaTiO_3$ metal–oxygen linkage remained intact following incorporation into PMMA [26]. $BaTiO_3$ nanoparticles generally exhibited strong lattice absorption peak near 570–578 cm^{-1} for Ti–O stretching within $BaTiO_3$ structure [25], [27]. The bands at 543 cm^{-1} for 20 wt% BTO/PMMA and 741 cm^{-1} for 30 wt% BTO/PMMA were attributed, related to lattice vibrations, with the higher-wavenumber region potentially influenced by PMMA skeletal vibrations. The bands at 734 and 848 cm^{-1} were associated with CH_2 rocking and skeletal vibration modes of PMMA, indicating that the polymer backbone was preserved following ceramic incorporation [28]. The absorption bands at 1009 cm^{-1} and 1167 cm^{-1} for the 20 wt% BTO/PMMA composite, and at 997 cm^{-1}, 1138 cm^{-1}, and 1255 cm^{-1} for the 30 wt% BTO/PMMA composite, were assigned to ester-related C–O–C stretching vibrations of PMMA. The PMMA ester groups were detected by a C=O stretching mode near 1730 cm^{-1} and C-O-C stretching mode near 1191 cm^{-1} and 1149 cm^{-1}, respectively [29]. The small shifts in the bands provided the evidence for the differences in the local environment of the ester groups due to the interactions at the BTO-PMMA interface [30]. The bands at 1449 cm^{-1} and 1433 cm^{-1} were mainly attributed to CH_3 bending vibration bands of the PMMA, with a smaller contribution from carbonate species in this region [31], [32]. BTO/PMMA nanocomposites 20 and 30 wt% compositions showed the band at 1712 cm^{-1} and 1725 cm^{-1}. Both bands were assigned to the C=O stretching vibrations within PMMA polymer. The shifts of the bands were caused by the change in the carbonyl environment due to the interaction between the PMMA matrix and the BTO surface [33]. The bands at 2942 cm^{-1} and 2937 cm^{-1} were

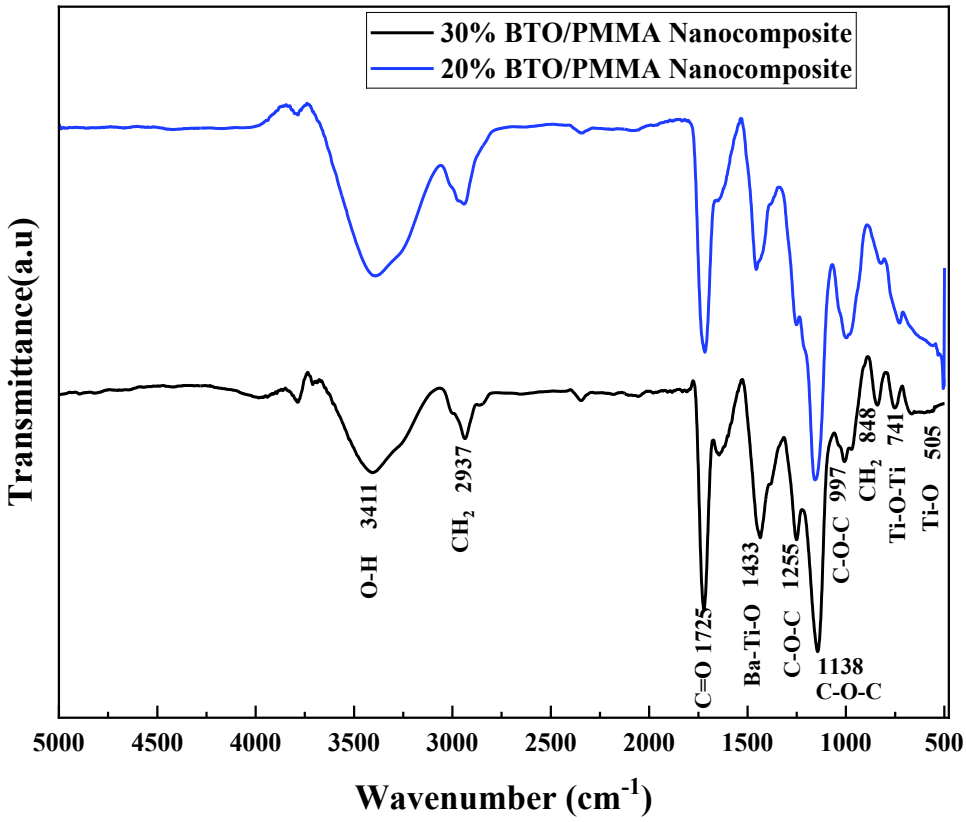


Figure 3.2. FTIR spectra for 20 wt% and 30 wt% BTO/PMMA nanocomposites

demonstrated due to C-H stretching of CH_2/CH_3 C groups in PMMA . The broad band at 3411 cm^{-1} was attributed to O-H stretching vibrations of the surface adsorbed hydroxyl groups from water molecules of BTO nanoparticles [25], [29].

Table 3.1. FTIR band positions, vibrational assignments, and main origins of pure BTO nanocomposites

Wavenumber (cm^{-1})	Interpretation
526	Ti–O stretching
854	Ti–O–Ti vibration
1430	CO_3^{2-} asymmetric stretching
3776	O–H stretching

Table 3.2. FTIR band positions, vibrational assignments, and main origins of BTO/PMMA nanocomposites

20% BTO/PMMA Nanocomposite Wavenumber (cm^{-1})	30% BTO/PMMA Nanocomposite Wavenumber (cm^{-1})	Interpretation
505	505	Ti–O stretching of (TiO_6 octahedra)
543	741	Ti–O–Ti lattice vibration
734	848	CH_2 rocking
824	997	Ba–Ti–O lattice vibration overlapping with C–O–C stretching
1009	1138	C–O–C stretching
1167	1255	C–O–C asymmetric stretching
1449	1433	CH_3 bending
1712	1725	C=O stretching
2942	2937	CH_2 stretching
3411	3411	O–H stretching

3.1.2. XRD Analysis

3.1.2.1. Major Peak Analysis

Figure 3.3 displays the X-ray diffraction pattern of $BaTiO_3$ powder calcined at 800 °C for 1 hour. Diffraction data were collected over a 2θ range of 10–80° with a step width of 0.02°, using Cu Kα radiation (wavelength 0.1540 nm) at an operating voltage of 40 kV and a current of 30 mA. Distinct diffraction peaks were observed at 2θ values of 22.161°, 31.638°, 39.047°, 45.209°, 50.967°, 56.288°, 66.076°, and 74.905°, corresponding to the (001), (101), (111), (002), (102), (112), (202), and (103) crystallographic planes, respectively. The observed peak positions are in good agreement with the standard diffraction pattern of tetragonal $BaTiO_3$ reported in JCPDS card no. 01-075-2118, confirming the formation of the perovskite BTO phase. No additional diffraction peaks attributable to detectable secondary crystalline phases were observed within the resolution of the measurement, indicating the successful formation of $BaTiO_3$ under the applied synthesis and calcination conditions. The sharp and well-defined diffraction peaks further demonstrate the highly crystalline nature of the synthesized powder. Among the observed reflections, the peak located at 2θ = 31.638°, assigned to the (101) plane, exhibited the highest intensity and represents the dominant reflection of the synthesized BTO nanoparticles. The crystallinity index was estimated

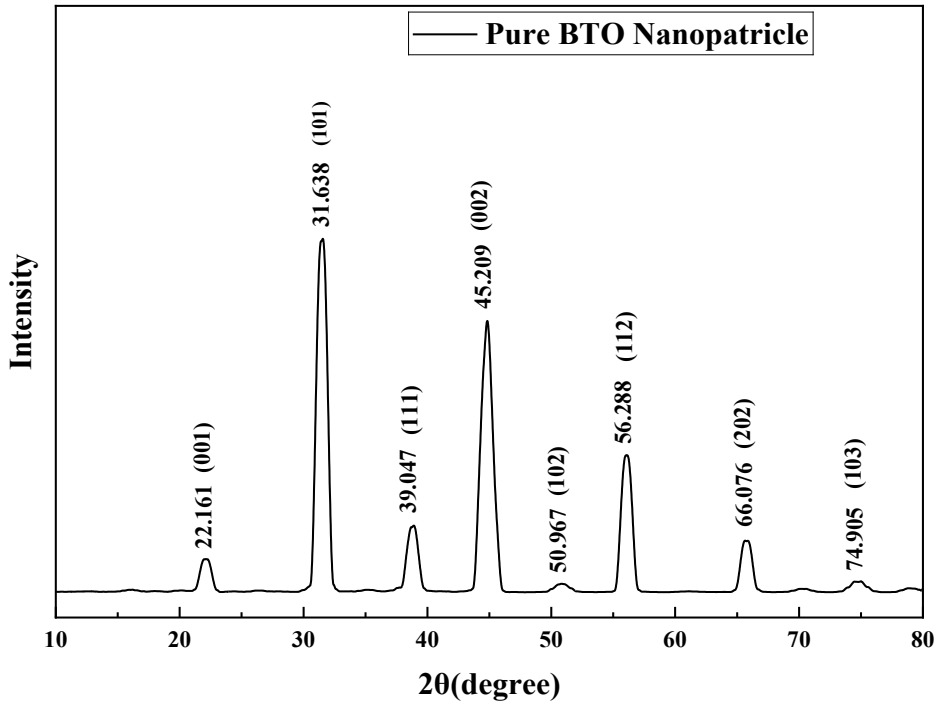


Figure 3.3: X-ray diffraction (XRD) pattern of pure BTO nanoparticles.

to be approximately 88.94%, which is consistent with the pronounced diffraction peaks observed in the XRD pattern. Overall, the results confirm the formation of highly crystalline $BaTiO_3$ nanoparticles with no detectable major impurity phase.

3.1.2.2. Williamson–Hall Analysis: Crystallite Size and Microstrain

The average crystallite size and lattice microstrain of the synthesized BTO nanoparticles were determined using Williamson–Hall analysis according to the Uniform Deformation Model. This method considers the broadening of the diffraction peaks resulting from the combined contributions of finite crystallite size and strain developed within the crystal lattice. The model assumes that the strain is uniformly distributed along the different crystallographic directions. Figure 3.4 presents the Williamson–Hall plot, which was constructed using the experimental full width at half maximum values of the major diffraction peaks. This analytical method is consistent with the structural interpretation described in the supplied reference paper. Linear fitting of the Williamson–Hall plot resulted in an average crystallite size of approximately 14.49 nm and an average microstrain of 0.63×10^{-3}. The relatively low microstrain indicates a limited degree of average lattice distortion within the calcined $BaTiO_3$ crystallites. The crystallite size determined from XRD was smaller than the average particle size of approximately 37 nm obtained from SEM analysis. This difference suggests that the particles observed in the SEM micrograph consist of multiple smaller coherently diffracting crystallites or closely associated nanocrystals. The result is

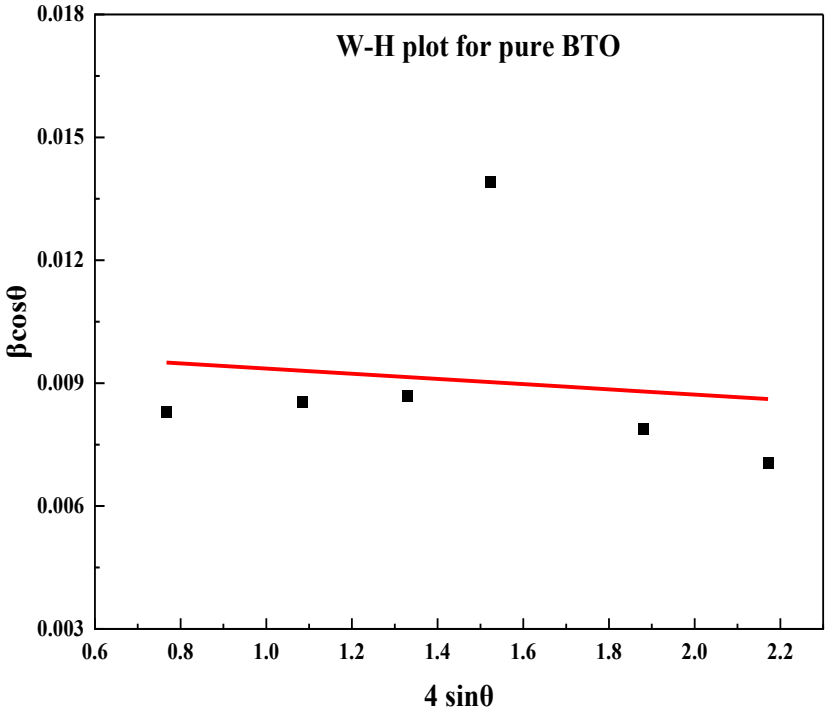


Figure 3.4: Williamson–Hall plot for pure BTO nanoparticles.

also consistent with the agglomerated and clustered morphology observed in the synthesized BTO powder.

Table 3.3. Summary of the structural and optical parameters of the synthesized $BaTiO_3$ nanoparticles

Sample name	2θ of (101) peak	Crystallite size (nm)	Average micro Strain ($\times 10^{-3}$)	Crystallinity index in %	Bandgap Energy (eV)
BaTiO3	31.64	14.49	0.63	88.94	2.92

3.2. Morphology analysis

3.2.1. SEM Analysis

SEM characterization was conducted to determine the morphology of the synthesized BTO nanoparticles (NPs), as this property significantly affects their dispersion and interfacial behavior in polymer nanocomposites. Figure 3.5 shows that the nanoparticles exhibit predominantly irregular to quasi-spherical morphologies with a relatively non-uniform distribution. Noticeable agglomeration and the formation of particle clusters are evident in several regions. The average particle size and particle-size distribution were measured using ImageJ and OriginLab Pro software, respectively, also shown in Figure 3.5. SEM analysis indicates an average particle size of approximately 37 nm.

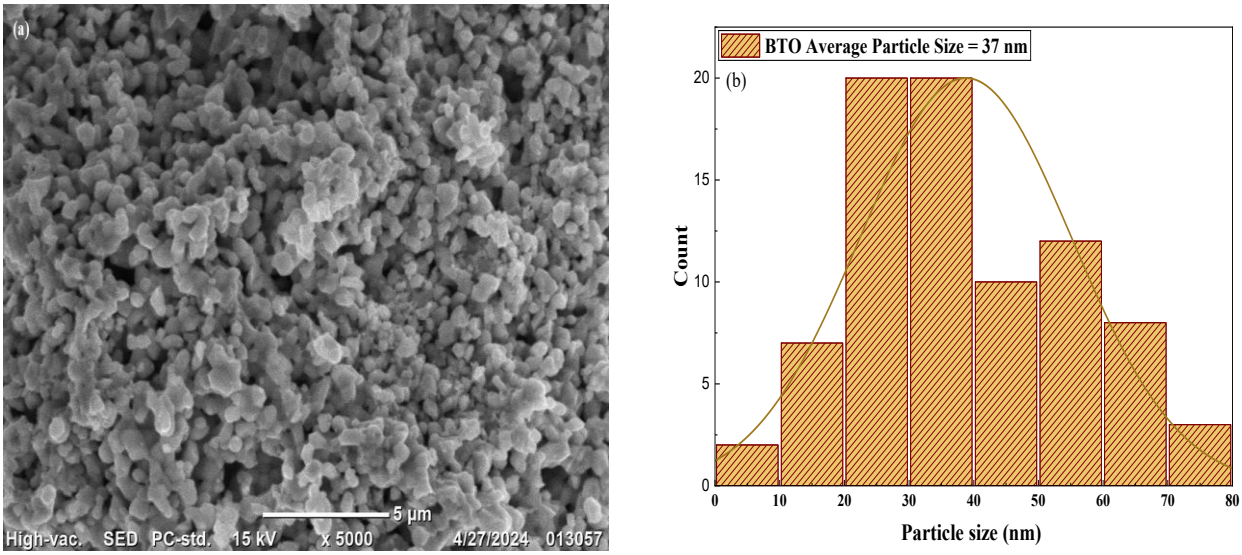


Figure 3.5. Morphology and particle size distribution of $BaTiO_3$ nanoparticles (a) SEM micrograph and (b) Particles size distributions of $BaTiO_3$ nanoparticles

3.3. UV-Vis Analysis

3.3.1. Band-gap Analysis

UV-Vis spectroscopy is employed to evaluate the optical properties of materials by measuring their absorption of ultraviolet and visible light. The optical properties of the synthesized BTO nanoparticles were examined using a UV–visible spectrometer [UV-2600, SHIMADZU]. The absorbance spectrum presented in Figure 3.6 (a) demonstrates substantial absorption in the ultraviolet region. The band-gap energy was analyzed from the absorbance data using the Tauc plot method [34]:

$$(\alpha h\nu)^{\gamma} = A(h\nu - E_g)$$

Here, α denotes the absorption coefficient, h is Planck's constant, ν represents the photon frequency, A is the proportionality constant, and E_g is the optical band-gap energy. The γ value can be 1/2 for indirect allowed transitions and $\gamma = 2$ for direct allowed transitions. Figure 3.6 (b) presents the indirect band-gap energy of the synthesized BTO nanoparticles, which was found to be 2.92 eV, using $\gamma = 1/2$ for this indirect band gap. This value is marginally lower than the band-gap energies of about 3.18 eV and 3.12 eV reported for the tetragonal and cubic phases of bulk $BaTiO_3$, respectively [35]. Oxygen vacancies and associated Ti^{3+} defects can introduce additional in-gap electronic states in the BTO structure [36]. Furthermore, lattice strain and structural disorder in the synthesized nanoparticles, as indicated by Williamson–Hall and XRD data, may also contribute to the observed band-gap reduction.

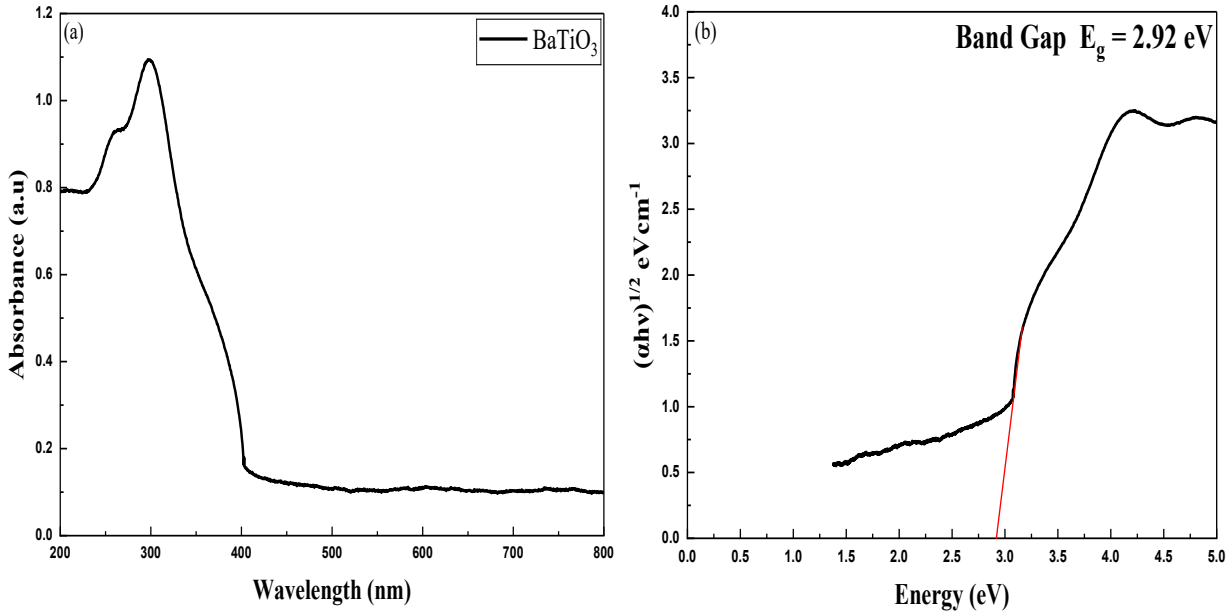


Figure 3.6. (a) UV–Vis absorbance spectrum of the synthesized $BaTiO_3$ nanoparticles (b) Tauc plot showing the direct band-gap energy of the synthesized $BaTiO_3$ nanoparticles

3.3.2. Photocatalytic Performance Evolution

The photocatalytic activity of BTO/PMMA nanocomposites was assessed by monitoring the photodegradation of methylene blue (MB) under ultraviolet (UV) irradiation for 75 minutes, as illustrated in Figure 3.7. The absorption spectrum of the MB solution displayed two characteristic peaks at 612 nm and 663 nm. Photodegradation was tracked at 663 nm, which corresponds to the main visible absorption band of MB. The absorbance at 663 nm progressively decreased with longer UV irradiation, indicating ongoing decolorization of the dye solution.

The 30 wt% BTO/PMMA nanocomposite showed enhanced light-harvesting behavior, as indicated by its stronger UV absorption. This enhancement was attributed to larger surface area of BTO/PMMA which provided more active sites and inhibited electron-hole pair recombination [7], [8], [19]. This observation is consistent with previous findings that the metal-oxide particles reinforcement into PMMA polymer matrices enhances dye removal of photocatalytic system, attributing enhanced surface properties, increased pollutant adsorption, and greater accessibility of active species through π-π stacking and ionic interaction [8], [21]. Under UV irradiation, $BaTiO_3$ acted as the photoactive semiconductor and generated electron–hole pairs. The synthesized BTO nanoparticles exhibited a band-gap energy of 2.92 eV, which enabled UV-light absorption and the subsequent formation of reactive oxygen species, including hydroxyl radicals (•OH), through surface redox reactions [7], [37]. These reactive species attacked the conjugated chromophoric structure of MB and promoted dye decolorization. In the BTO/PMMA nanocomposites, PMMA primarily served as a supporting and immobilizing matrix, whereas BTO provided the active semiconductor sites required for photon absorption and interfacial redox reactions [19], [21]. The

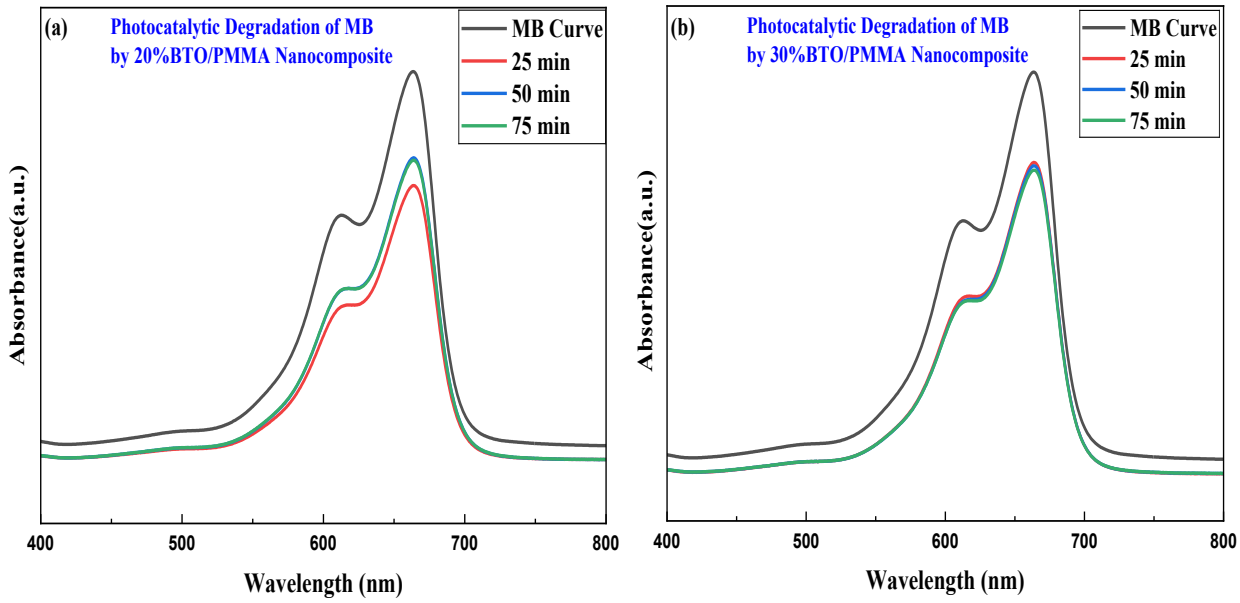


Figure 3.7. Time-dependent absorbance spectra of MB in the presence of (a) 20 wt% BTO/PMMA and (b) 30 wt% BTO/PMMA nanocomposites.

improved degradation performance was therefore attributed to the efficient reactive species generation and the availability of photocatalytically active sites under UV irradiation.

3.3.2.1. Effect of BTO nanoparticle reinforcement

A clear composition-dependent trend emerged over the 75 min irradiation period. At 25, 50, and 75 min, degradation efficiencies were 21.57%, 22.32%, and 22.87% for the 20 wt% composite and

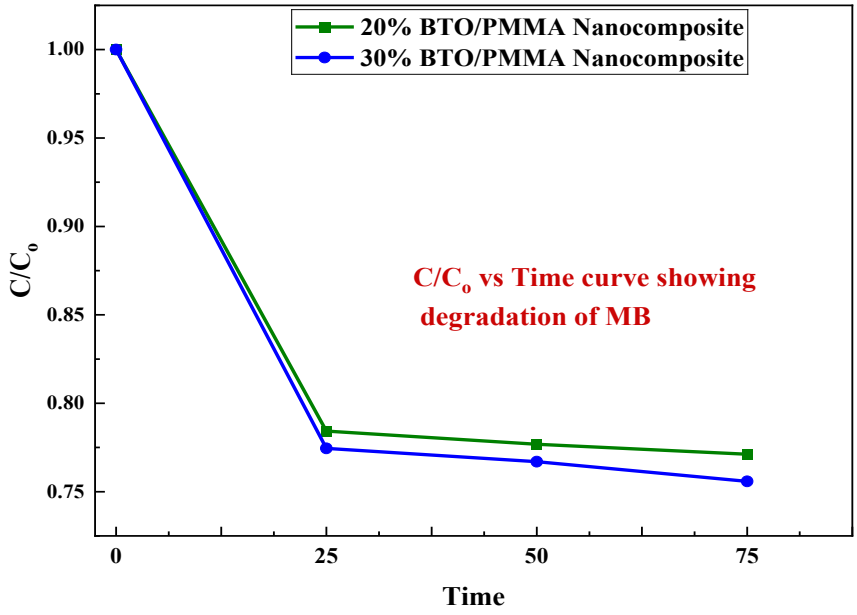


Figure 3.8. Plot of (C/C_0) versus irradiation time showing the photodegradation of methylene blue over the 20 wt% and 30 wt% BTO/PMMA nanocomposites under light irradiation.

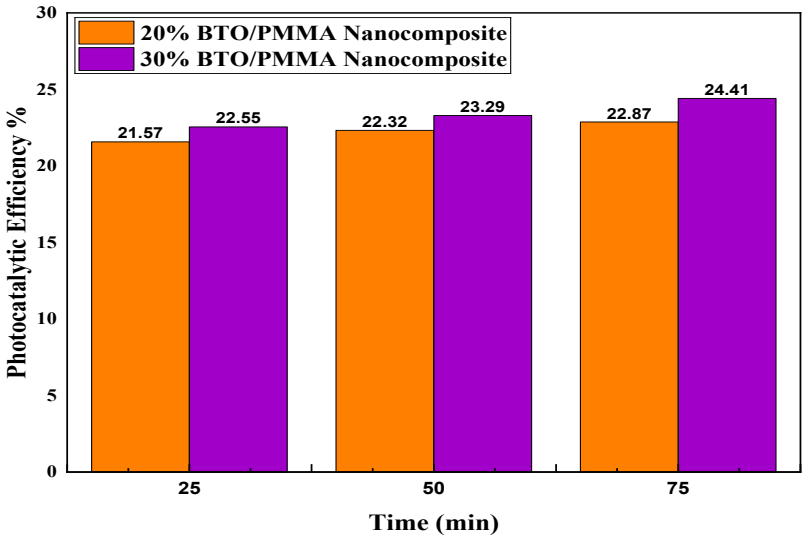


Figure 3.9. Photocatalytic degradation efficiencies of the 20 and 30 wt% BTO/PMMA nanocomposites.

22.55%, 23.29%, and 24.41% for the 30 wt% composite, respectively. As summarized in Figures 3.8 and 3.9, the degradation efficiency increased modestly when the BTO reinforcement was increased from 20 to 30 wt%. Thus, among the investigated compositions, the 30 wt% BTO/PMMA nanocomposite exhibited the highest measured photocatalytic performance. Increasing the BTO content increased the photoactive ceramic fraction and the number of BTO/PMMA interfaces. These interfaces supported BTO dispersion and provided additional sites for photon absorption, electron–hole generation, and surface redox reactions, consistent with the reported influence of polymer–ceramic interfacial interactions [19], [21]. For determining photocatalytic degradation efficiency, the efficiency equation was calculated as follows [38]:

$$Efficiency\ (\%) = \frac{C_o - C_t}{C_o} \times 100$$

Where C_o is the initial concentration and C_t is the dye concentration at irradiation time.The degradation efficiency of photocatalytic activity is important, as long-term stability and durability of a photocatalytic material can be determined through this calculation [39]. Furthermore, quantifying the degradation efficiency of photocatalytic activity is essential for precise assessment of the photocatalyst's performance over time [40]. If degradation efficiency is not considered, the reported photocatalytic activity efficiency may be misleading and fail to reflect the actual performance of the nanocomposites in practical applications. [41].

3.3.2.2. Degradation kinetics

The degradation kinetics of MB in the presence of the BTO/PMMA nanocomposites were analyzed using the pseudo-first-order model described by equation:

$$\ln\left(\frac{C_t}{C_0}\right) = -kt$$

Here, C_0 is the initial concentration of dye, C_t represents the concentration of dye at time 't', 'k' is the first order rate constant, which was calculated from the slope of the straight line obtained by plotting -ln(C/Co) vs time, in Figure 3.10 [7], [8]. The fitted pseudo-first-order rate constants (k) and the corresponding coefficients of determination (R^2) were summarized in Table 3.4. Among the investigated compositions, the 30 wt% BTO/PMMA nanocomposite exhibited the highest apparent rate constant. The apparent rate constant followed a clear trend, increasing from (0.00316 ± 0.00163) min^{-1} at 20 wt% BTO/PMMA to (0.00340 ± 0.00168) min^{-1} at 30 wt% BTO/PMMA. This variation in 'k' was consistent with the degradation efficiencies and reflected enhanced photocatalytic performance at 30 wt% [41]. Nevertheless, the R^2 values of 0.65254 and 0.67145 indicated only moderate linear agreement with the pseudo-first-order model. Accordingly, the calculated rate constants were best interpreted as comparative kinetic indicators under the present test conditions rather than as definitive evidence of strict pseudo-first-order behavior.

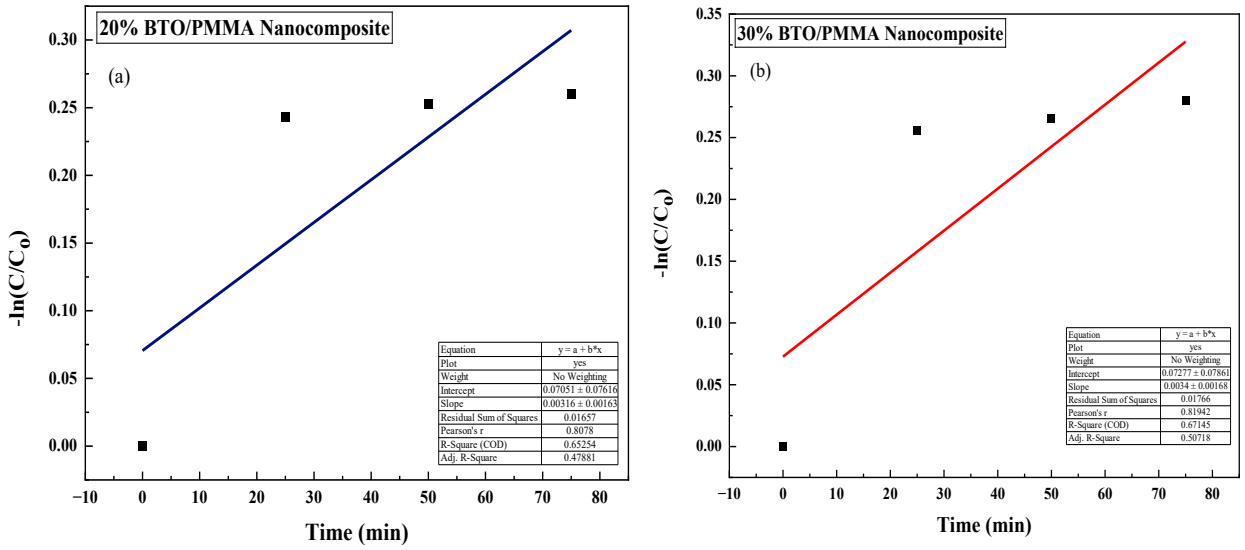


Figure 3.10. Pseudo-first-order kinetic plots of ln(C/C0) versus irradiation time for MB degradation in the presence of (a) 20 wt% and (b) 30 wt% BTO/PMMA nanocomposites.

Table 3.4. Pseudo-first-order kinetic parameters and degradation efficiencies of the BTO/PMMA nanocomposites.

Sample	C/C0 after 25 min	C/C0 after 75 min	k (min^{-1})	R^2	Efficiency (%) after 25 min	Efficiency (%) after 75 min
20 wt% BTO/PMMA nanocomposite	0.78425	0.77120	0.00316 ± 0.00163	0.65254	21.57	22.87
30 wt% BTO/PMMA nanocomposite	0.77446	0.75582	0.00340 ± 0.00168	0.67145	22.55	24.41

3.3.2.3. Proposed mechanism of degradation

In general, the photocatalytic process involves three principal steps: light absorption, generation of electron–hole pairs, and interfacial redox reactions mediated by charge transfer [7], [37]. Under UV irradiation, BTO serves as the photoactive component in the BTO/PMMA nanocomposite. In this role, electrons are promoted from the valence band (VB) to the conduction band (CB), resulting in the generation of electron–hole pairs [7]. PMMA functions as a supporting matrix, and its carbonyl and ester groups can interact with the BTO surface, assisting nanoparticle dispersion and improving the accessibility of photocatalytically active sites [21], [22]. The photogenerated charge carriers then migrate to the BTO surface, where CB electrons reduce adsorbed oxygen to superoxide radicals ($O_2^{\bullet-}$), while VB holes react with H_2O or OH^- to generate hydroxyl radicals ($^{\bullet}OH$). Protonation of $O_2^{\bullet-}$ produces hydroperoxyl radicals ($HO_2^{\bullet}$), which can subsequently form H_2O_2 and additional $^{\bullet}OH$. The combined action of photogenerated holes, $O_2^{\bullet-}$, and $^{\bullet}OH$ attacks the conjugated chromophoric structure of MB, resulting in decolorization and the generation of intermediate degradation products. Based on the reported BTO photocatalytic pathways [7], [37], the proposed reactions are as follows:

$BTO/PMMA + h\nu \rightarrow BTO/PMMA\ (e^-(CB) + h^+(VB))$

$O_2 + e^-(CB) \rightarrow O_2^{\bullet-}$

$MB + e^-(CB) \rightarrow$ reduced intermediates

$H_2O + h^+(VB) \rightarrow H^+ + {}^{\bullet}OH$

$OH^- + h^+(VB) \rightarrow {}^{\bullet}OH$

$MB + h^+(VB) \rightarrow$ oxidized intermediates

$O_2^{\bullet-} + H^+ \rightarrow HO_2^{\bullet}$

$2HO_2^{\bullet} \rightarrow H_2O_2 + O_2$

$H_2O_2 + h\nu \rightarrow 2{}^{\bullet}OH$

$MB + (^{\bullet}OH, O_2^{\bullet-}, h^+) \rightarrow$ degradation intermediates/products

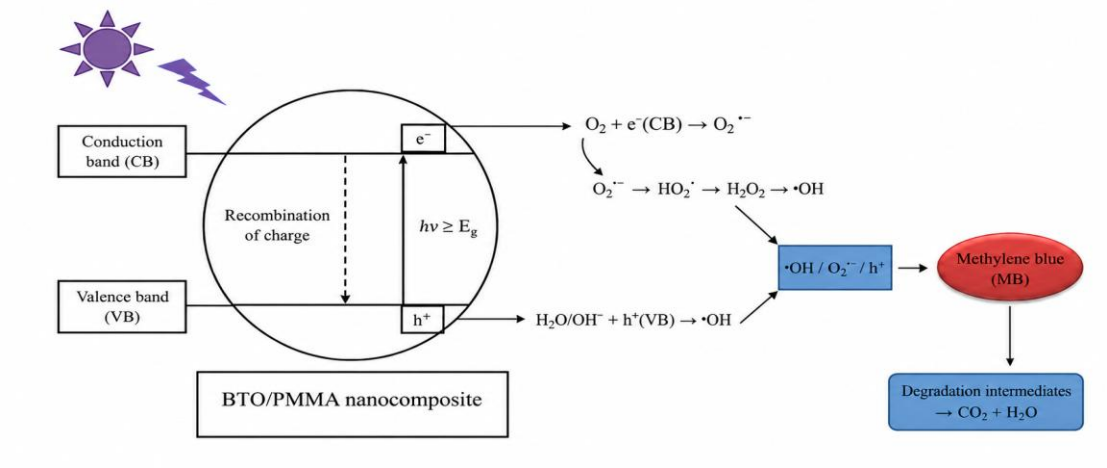


Figure 3.3.2.3.1. Illustration of proposed photocatalytic degradation mechanism of MB by BTO/PMMA nanocomposite

3.4. Piezoelectric Analysis

The piezoelectric coefficient (d_{33}) of BTO/PMMA nanocomposites were measured with YE2730A d_{33} Meter (Sinocera). This meter is able to measure the d_{33} values over a wide range, at better resolution with a high degree of reliability. As previously discussed, the incorporation of ceramic nanoparticles into polymer matrices could enhance the piezoelectric response by promoting electroactive-phase formation and interfacial polarization [42], [43], [44]. Figure 3.11 illustrated that 30wt% BTO/PMMA nanocomposite provided higher d_{33} value 37 pC/N than 20wt% BTO/PMMA nanocomposite showed 35 pC/N, respectively.

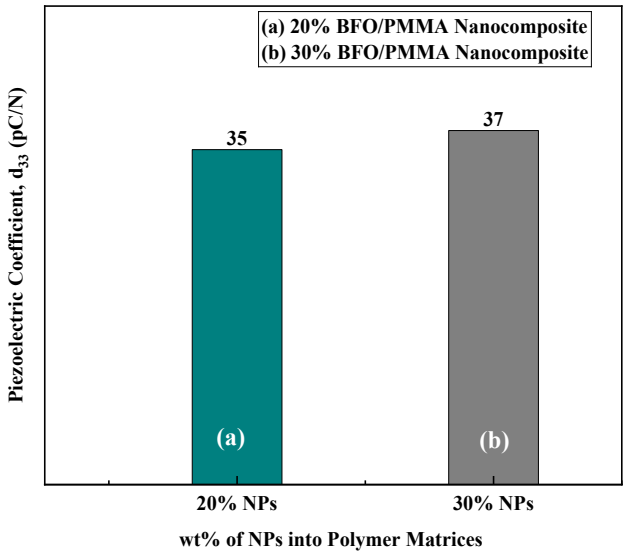


Figure 3.11. Comparison of piezoelectric coefficient (d_{33}) of BTO/PMMA nanocomposites for (a) 20wt%, and (b) 30wt% BTO NPs reinforced into Polymer matrices.

3.5. Electrical Properties Analysis

3.5.1. Dielectric Studies

Complex impedance spectroscopy is employed to investigate the electrical properties of electro-materials. This technique allows for effective analysis of the contributions of grains and grain boundaries to dielectric properties, including dielectric constant, dielectric loss, and conductivity. The frequency dependence of the dielectric constant (ε'), dielectric loss ($\tan\delta$), and conductivity (σ_{ac}) for nanocomposites with varying BTO contents is presented in Figure 3.12, Figure 3.13, and Figure 3.14. As shown in Fig. 1(a), the dielectric constant values of all nanocomposites were dependent on frequency over the considered range 40Hz-100MHz. The dielectric constants of nanocomposites were continuously increased with the BTO nanoparticles reinforcement [45], [46]. At 40 Hz, the dielectric constants of the 20 wt% BTO/PMMA and 30 wt% BTO/PMMA

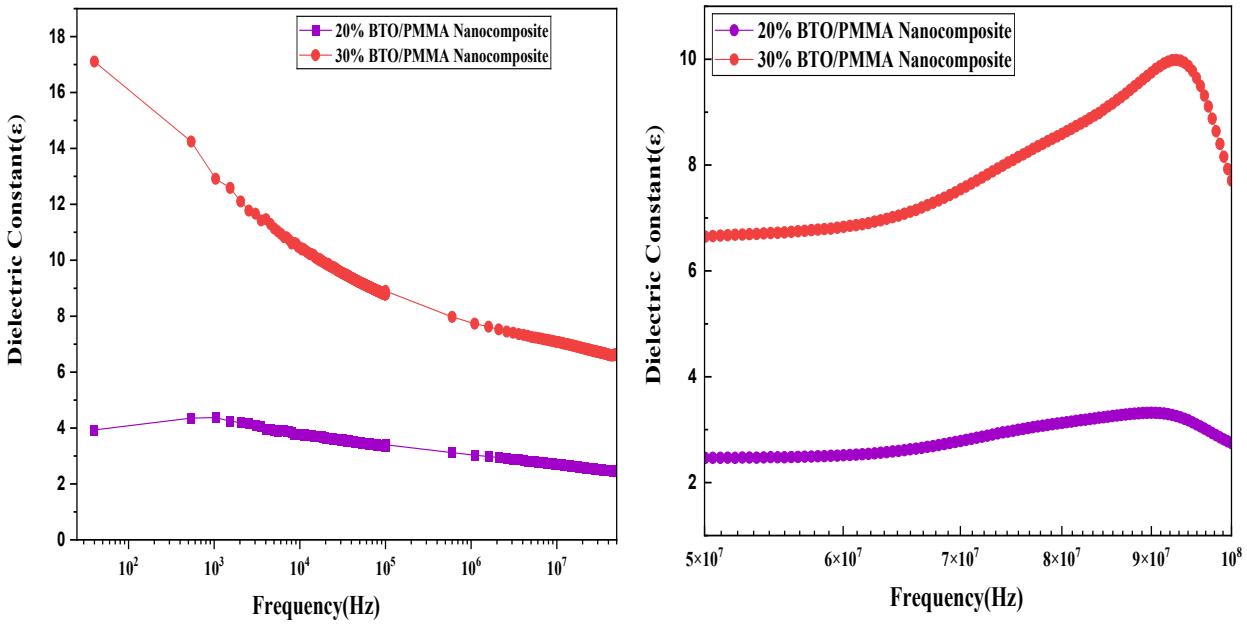


Figure 3.12. Dielectric constant of BTO/PMMA nanocomposites at 40-50MHz, and 50MHz-100MHz at room temperature

nanocomposites were approximately 3.93 and 17.11, respectively. This improvement is attributed to higher dielectric constant of BTO nanoparticles relative to PMMA matrix, and the Maxwell-Wagner-Sillars (MWS) interfacial polarization effect [47], [48], [49]. MWS interfacial polarization was prominent at low frequency region due to its relatively long relaxation time [50]. At 10 kHz, the corresponding values of 20 wt% BTO/PMMA and 30 wt% BTO/PMMA

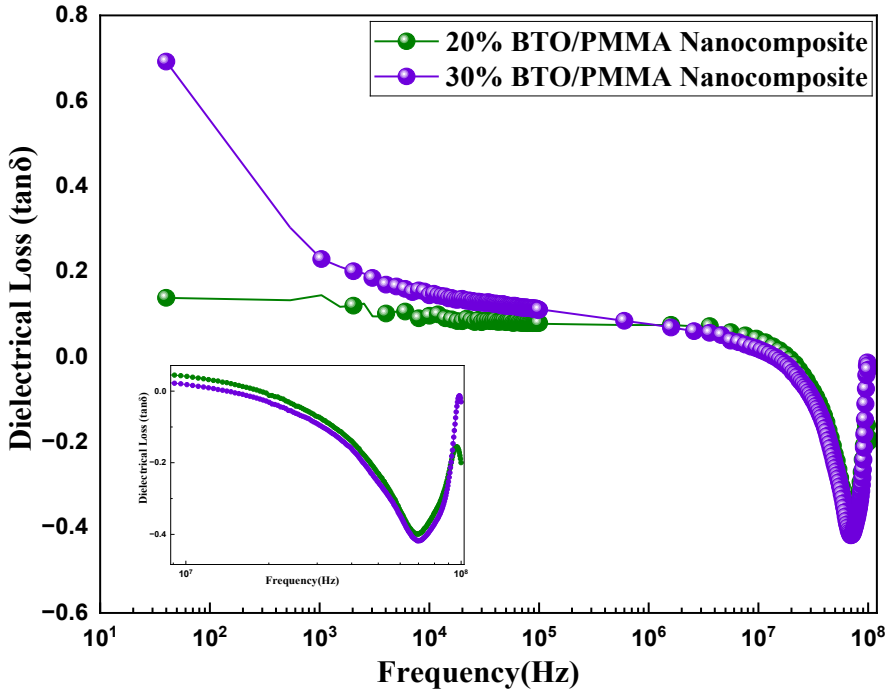


Figure 3.13. Dielectric loss of BTO/PMMA nanocomposites at 40-100MHz frequency region at room temperature

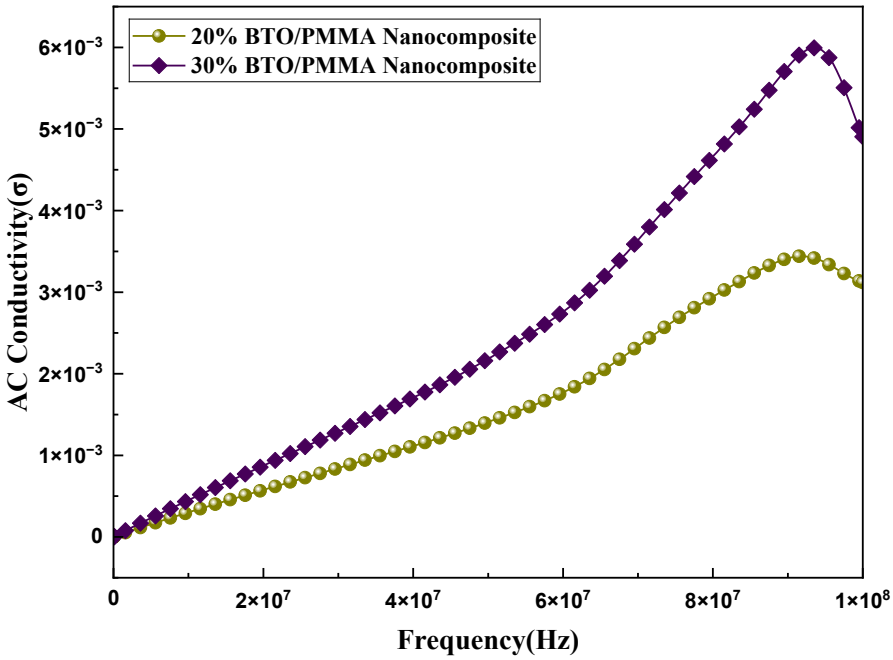


Figure 3.14. Frequency dependence of Ac conductivity at room temperature for 20 wt% and 30wt% nanocomposites

nanocomposites were approximately 3.8 and 10.6, whereas gradually decreased 2.8 and 7.2 for 10 MHz, respectively. As measurement frequency increased, dielectric constant decreased from 40 Hz to 100MHz. In contrast, a slight anomalous increase was observed for 30 wt% BTO/PMMA nanocomposite at high frequency range 93 MHz, where dielectric constant was 10, compared with 3.36 for 20 wt% BTO/PMMA nanocomposite.As shown in the inset of Figure 3.13, the low

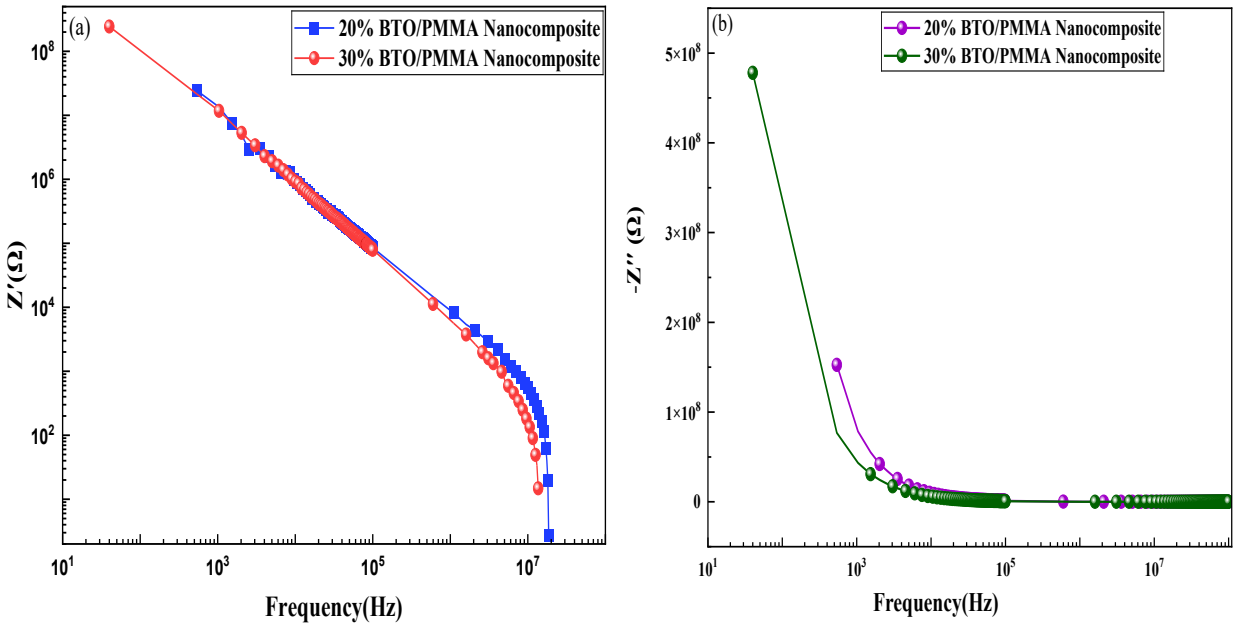


Figure 3.15. Variation of (a) real part modulus Z', and (b) imaginary part of modulus Z″ with frequency at a room temperature

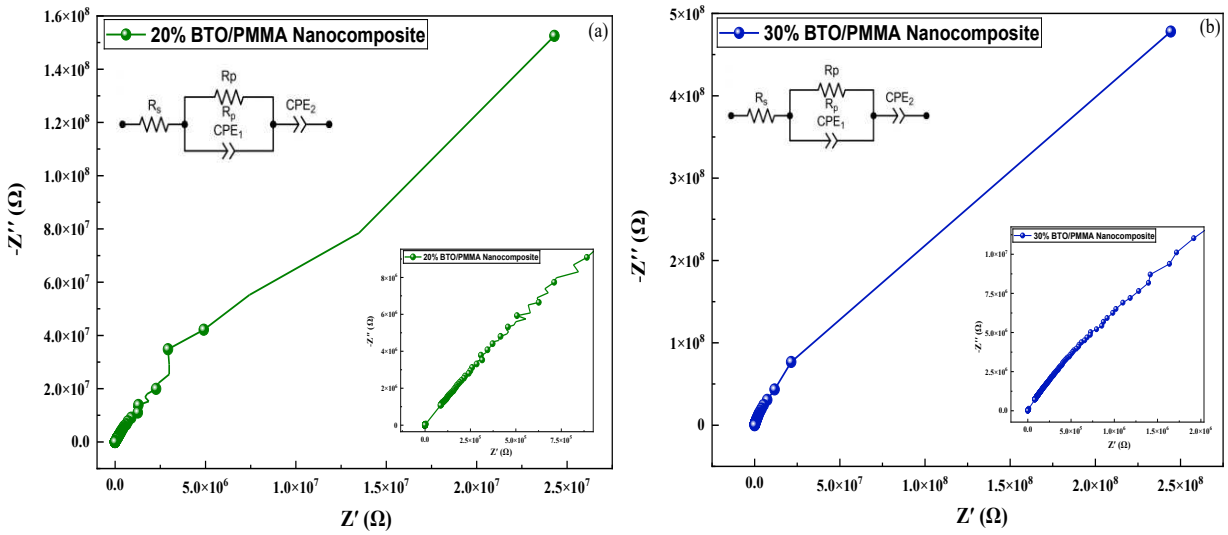


Figure 3.16. Complex impedance plots for the (Z″= f (Z^')) for the (a) 20wt% BTO/PMMA, and (b) 30wt% BTO/PMMA nanocomposites at 40Hz – 100MHz

frequency dielectric loss (loss tangent) of nanocomposites increased with 20 wt% to 30 wt% NPs reinforcement from 0.14 to 0.69. A similar decreasing trend in dielectric loss was observed with increasing frequency with a value of 0.05 and 0.04 at 10MHz for 20% BTO/PMMA and 30% BTO/PMMA nanocomposites, respectively, at room temperature, which was attributed to the suppression of electric dipole moment, as presented in Table 3.5 [50]. These results confirmed that the incorporation of BTO nanoparticles into PMMA matrices significantly enhances the dielectric performance of the resulting nanocomposites [51]. Figure 3.14 showed the frequency dependence of ac conductivity at room temperature for both nanocomposites. It was observed that the ac conductivity in the high-frequency range increased as the percentage of reinforced nanoparticles increased.. As summarized in Table 3.5, at room temperature and 1MHz, σ_{ac} of the BTO/PMMA nanocomposite increased slightly 0.02×10^{-3} S cm^{-1} to 0.03×10^{-3} S cm^{-1} with an increase of 20 wt% to 30 wt% BTO nanoparticles reinforcement into PMMA matrices, respectively, whereas σ_{ac} increased ($\approx0.35\times10^{-3}$ S cm^{-1}) to ($\approx0.45\times10^{-3}$ S cm^{-1}). It was worth noted that the conductivity of 20% BTO nanocomposites and 30% BTO nanocomposites attributed highest ($\approx3.42\times10^{-3}$ S cm^{-1}) and ($\approx5.98\times10^{-3}$ S cm^{-1}) at 90MHz high frequency, and gradually decreased at 100MHz. Here, conductivity increases with frequency for both filler concentrations in BTO/PMMA. The ac conductivity remains low in the low-frequency region and exhibits pronounced dispersion at higher frequencies [52]. As the BTO concentration increases from 20 to 30 wt%, conductivity increased with interfacial polarization and localized charge transport across the BTO/PMMA interfaces [17], [53].

3.5.2. Impedance analysis

Complex impedance spectroscopy was employed to investigate the electrical properties of BTO/PMMA nanocomposites across the frequency range of 40 Hz to 100 MHz at room temperature [54], [55]. Complex electric modulus analysis was conducted to examine the frequency dependence of the electrical response in BTO/PMMA nanocomposites [56]. In our

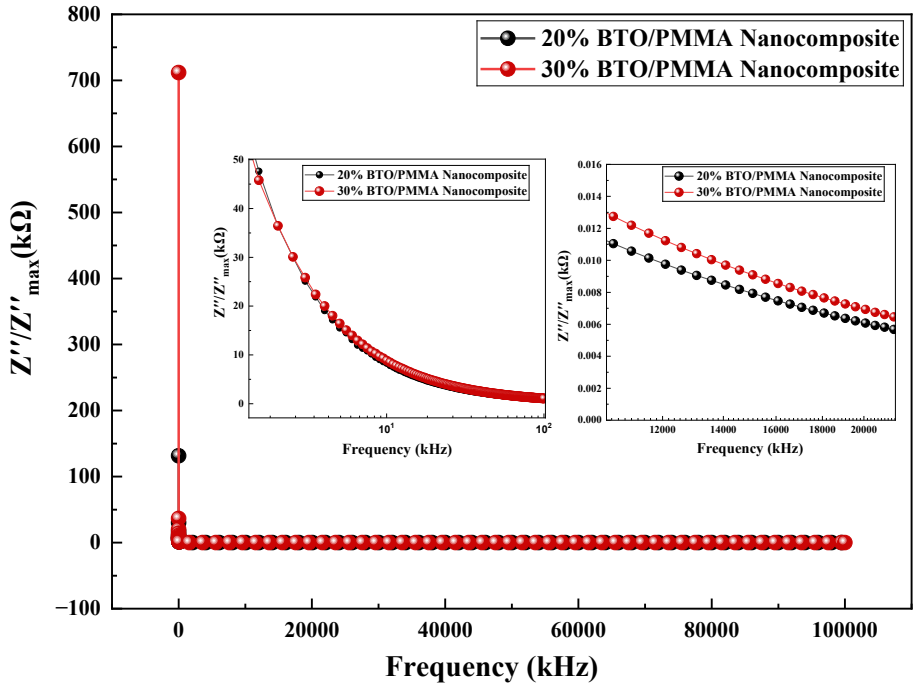


Figure 3.17. Normalized imaginary part of impedance (Z″/Z_max^″) with frequency of BTO/PMMA nanocomposites at room temperature.

analysis, we considered (1) series resistance (R_S), representing overall bulk resistance, is contributions of current collector, bulk electrode material, electrolyte and separator mediated resistance, (2) polarization resistance (R_P), which consisted of interfacial resistance (mainly SEI-mediated resistance, R_{SEI}), charge transfer resistance (R_{ct}), (3) Constant Phase Element (CPE_1), was placed with parallel with R_P, and (4) CPE_2 accounted for low frequency diffusive response [98-99]. Figure 3.15(a)-(b) presents the variation in real impedance (Z') and imaginary impedance

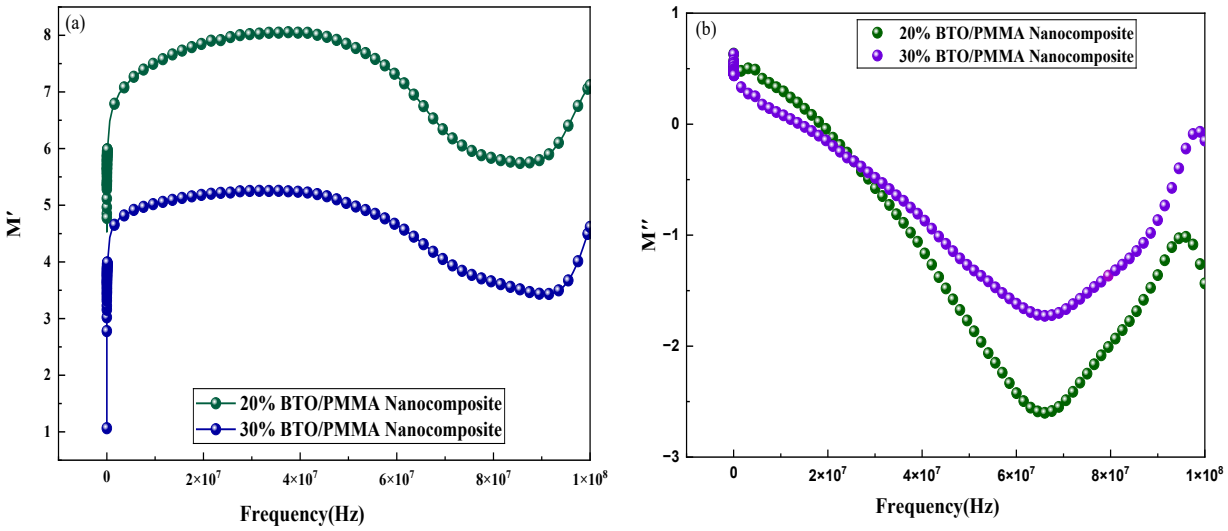


Figure 3.18. Variation of (a) real part modulus (M′) and (b) imaginary part modulus (M″) with frequency of BTO/PMMA nanocomposites at room temperature

(Z'') within the high-frequency range (40 Hz to 100 MHz). The magnitude of Z' decreases and the values converge as frequency increases. The observed decrease in Z' for both nanocomposite samples is attributed to the increase in alternating current (ac) conductivity with frequency. The convergence of impedance responses at high frequencies is ascribed to the release of space charges, which leads to reduced barrier properties within the nanocomposite [57], [58], [59]. It was observed that the initial value of Z'' might be indicated as Z''_{max} then it decreased as the frequency increased for both nanocomposite samples [60]. The 30 wt% BTO/PMMA nanocomposite exhibited the higher imaginary Z'' value in the low frequency range, which decreased gradually over higher frequency region because of space-charge polarization and interfacial polarization [45], [61]. The plot of Z' versus Z'' (Nyquist plot) at low to high frequency range was shown in Figure. 3.16, which expressed a single depressed semicircular arc confirmed deviation from Debye behavior with a distribution of relaxation time. This behavior was associated with heterogeneous interfaces and multiple polarization process of nanocomposites. The normalized imaginary part of impedance Z''/Z''_{max} as a function of frequency for both BTO/PMMA nanocomposites exhibited a broad relaxation response, indicating deviation from ideal-Debye type relaxation, plotted in Figure. 3.17. This behavior attributed to the heterogeneous BTO/PMMA interfaces and multiple polarization process [62], [63].

3.5.3. Modulus analysis

Figure 3.18(a) illustrated the frequency dependence of the real part of electric modulus M' for both BTO/PMMA nanocomposites. The 20 wt% BTO/PMMA nanocomposite exhibited a higher magnitude of M' compared to the 30 wt% BTO/PMMA nanocomposite across the frequency range. In the very low frequency region, the magnitudes of M' tended to zero, which evaluated a lower contribution of electrode effect. It exhibited continuous frequency dependent dispersion, suggested

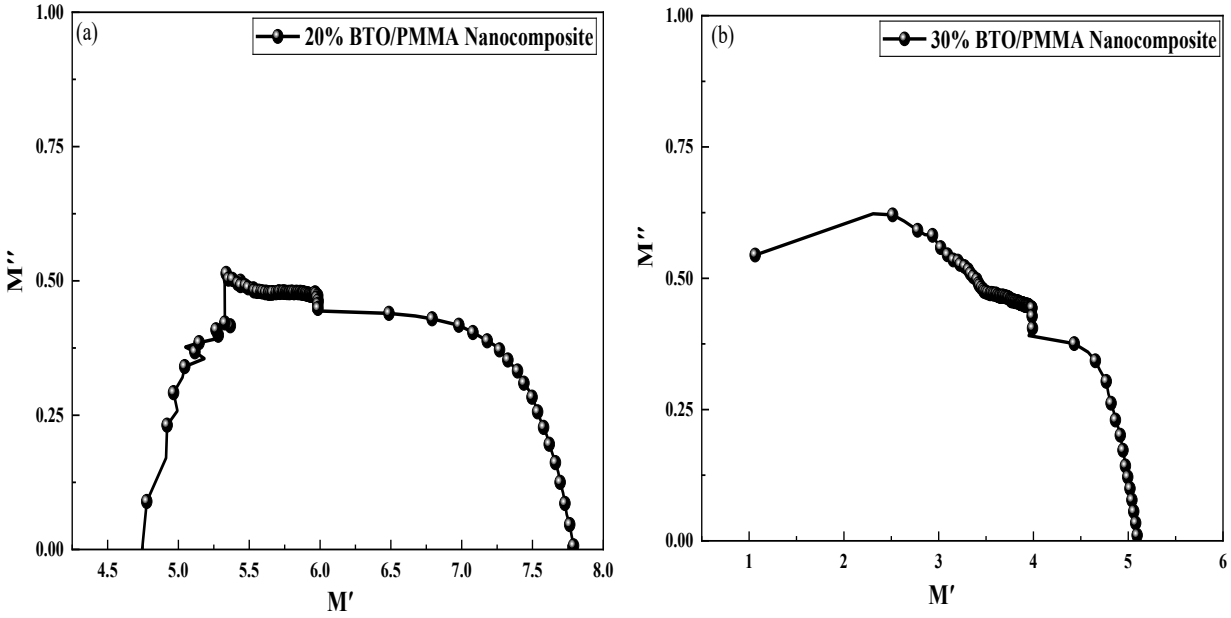


Figure 3.19. Nyquist plots of imaginary part modulus M'' vs real part modulus M' of (a) 20wt% BTO/PMMA, and (b) 30wt% BTO/PMMA nanocomposites

short-range mobility of charge carriers. With the increase of frequency, the M′ attained the (M'_{max}) value in the intermediate-frequency region and decreased gradually at high frequency region. Besides, a pronounced dispersion was observed at high frequency region, which indicated the contribution of localized charge-carrier relaxation process within nanocomposite samples [64]. Figure 3.18(b) represented the frequency dependence variation of imaginary part of electric modulus M″ for 20wt% and 30wt% BTO/PMMA nanocomposites. Both nanocomposites exhibited a broad negative peak in M''_{max}, indicating frequency dependent dielectric relaxation. The higher M″ response of 30wt% BTO/PMMA nanocomposite sample, together with its enhanced ac conductivity, suggested composition dependent relaxation and charge transport behavior [65]. Figure. 3.19. showed M″ vs M′ graph for both BTO/PMMA nanocomposites. The asymmetric semi-circular diagrams confirmed the presence of electrical relaxation phenomenon in the materials [45].

Table 3.5: Summary of the dielectric constant, dielectric loss, and AC conductivity of BTO/PMMA nanocomposites

Sample	Frequency range	ε′	tanδ	$\sigma_{ac} \times 10^{-3}$ (S/cm)
20 wt% BTO/PMMA Nanocomposite	40–1kHz	4.35	0.14	0.01
	1k–100 kHz	4.37	0.14	0.02
	100k–1 MHz	3.40	0.08	0.04
	1M–11O MHz	3.36	0.07	3.5
30 wt% BTO/PMMA Nanocomposite	40–1kHz	17.11	0.69	0.02
	1k–100 kHz	12.91	0.23	0.03
	100k–1 MHz	8.90	0.11	0.05
	1M–11O MHz	9.98	0.08	5.9

4. CONCLUSION

This study clarified how BTO nanoparticles concentration enhanced the functional behavior of solution-cast BTO/PMMA nanocomposites. Structural analysis as FTIR and XRD established the formation of crystalline tetragonal BTO and its successful incorporation into PMMA, while SEM ensured nanoparticles morphology. Increasing the BTO nanoparticles reinforcement from 20 wt% to 30 wt% increased the proportion of the polarizable ceramic phase and the density of heterogeneous interfaces, resulting in higher dielectric and better piezoelectric response with

notably high frequency-dependent ac-conductivity. The 30 wt% BTO/PMMA nanocomposite demonstrated highest photocatalytic activity for greater availability of photoactive BTO sites. The degradation of MB demonstrates its usefulness in waste management. Besides, 30 wt% composition exhibited enhanced piezoelectric performance which is potential for sensor and actuator applications. Such these nanocomposites with low reinforcement percentage have significant impact and offer new opportunities for designing scalable, high-energy-density polymer dielectric materials.

Declaration of generative AI and AI-assisted technologies in the manuscript preparation process

During the preparation of this work, the authors used generative AI tools (ChatGPT, OpenAI, and Gemini by Google) to assist with language refinement, clarity improvement, and organization of the manuscript text. These AI tools were not used to generate scientific results, data, analyses, figures, or interpretations. All AI-assisted content was thoroughly reviewed, edited, and validated by the authors to ensure accuracy, originality, and scientific integrity. The authors take full responsibility for the content of the published article.

Funding Declaration

The authors declare that no funds, grants, or other financial support were received from any organization or funding agency for the research, authorship, and/or publication of this article.

REFRENCES

[1] A. Parija, K. K. Das, U. A. Mohanty, and K. Parida, “Multifunctional PVDF based composite for sustainable catalysis: Insights into piezo-photocatalytic environmental and energy application,” *Chem. Eng. J.*, vol. 522, p. 167260, 2025, doi: https://doi.org/10.1016/j.cej.2025.167260.

[2] J.-W. Zha, M.-S. Zheng, B.-H. Fan, and Z.-M. Dang, “Polymer-based dielectrics with high permittivity for electric energy storage: A review,” *Nano Energy*, vol. 89, p. 106438, 2021, doi: https://doi.org/10.1016/j.nanoen.2021.106438.

[3] P. Barber *et al.*, “Polymer Composite and Nanocomposite Dielectric Materials for Pulse Power Energy Storage,” *Materials (Basel).*, vol. 2, no. 4, pp. 1697–1733, 2009, doi: 10.3390/ma2041697.

[4] M. Kober *et al.*, “Ferroelectric Properties of Polymer–Semiconductor Hybrid Material or Composite under Optical Excitation,” *Polymers*, vol. 16, no. 7. p. 929, 2024. doi: 10.3390/polym16070929.

[5] K. Suematsu, M. Arimura, N. Uchiyama, and S. Saita, “Transparent BaTiO3/PMMA Nanocomposite Filmsfor Display Technologies: Facile Surface Modification Approach forBaTiO3 Nanoparticles,” *ACS Appl. Nano Mater.*, vol. 1, no. 5, pp. 2430–2437, May 2018, doi: 10.1021/ACSANM.8B00650.

[6] M. Zgonik *et al.*, “Dielectric, elastic, piezoelectric, electro-optic, and elasto-optic tensors of ${\mathrm{BaTiO}}_{3}$ crystals,” *Phys. Rev. B*, vol. 50, no. 9, pp. 5941–5949, Sep. 1994, doi: 10.1103/PhysRevB.50.5941.

[7] D. K. Bhat, H. Bantawal, and U. S. Shenoy, “Rhodium doping augments photocatalytic activity of barium titanate: effect of electronic structure engineering,” *Nanoscale Adv.*, vol.

2, no. 12, pp. 5688–5698, Dec. 2020, doi: 10.1039/d0na00702a.

[8] Z. Mengting *et al.*, "Applicability of BaTiO3/graphene oxide (GO) composite for enhanced photodegradation of methylene blue (MB) in synthetic wastewater under UV–vis irradiation," *Environ. Pollut.*, vol. 255, p. 113182, 2019, doi: https://doi.org/10.1016/j.envpol.2019.113182.

[9] P. Eltouby, I. Shyha, C. Li, and J. Khaliq, "Factors affecting the piezoelectric performance of ceramic-polymer composites: A comprehensive review," *Ceram. Int.*, vol. 47, no. 13, pp. 17813–17825, 2021, doi: https://doi.org/10.1016/j.ceramint.2021.03.126.

[10] R. Yanagawa, M. Senna, C. Ando, H. Chazono, and H. Kishi, "Preparation of 200 nm BaTiO3 Particles with their Tetragonality 1.010 Via a Solid-State Reaction Preceded by Agglomeration-Free Mechanical Activation," *J. Am. Ceram. Soc.*, vol. 90, no. 3, pp. 809–814, Mar. 2007, doi: https://doi.org/10.1111/j.1551-2916.2007.01498.x.

[11] S. Gross, D. Camozzo, V. Di Noto, L. Armelao, and E. Tondello, "PMMA: A key macromolecular component for dielectric low-κ hybrid inorganic–organic polymer films," *Eur. Polym. J.*, vol. 43, no. 3, pp. 673–696, 2007, doi: https://doi.org/10.1016/j.eurpolymj.2006.12.012.

[12] A. Wypych-Puszkarz *et al.*, "Molecular Dynamics and Structure of Poly(Methyl Methacrylate) Chains Grafted from Barium Titanate Nanoparticles," *Molecules*, vol. 27, no. 19. p. 6372, 2022. doi: 10.3390/molecules27196372.

[13] K. Brandt, C. Neusel, S. Behr, and G. A. Schneider, "Dielectric behaviour and conductivity of high-filled BaTiO3–PMMA composites and the facile route of emulsion polymerization in synthesizing the same," *J. Mater. Chem. C*, vol. 1, no. 18, pp. 3129–3137, May 2013, doi: 10.1039/c3tc30204k.

[14] L. Xie, X. Huang, C. Wu, and P. Jiang, "Core-shell structured poly(methyl methacrylate)/BaTiO3 nanocomposites prepared by in situ atom transfer radical polymerization: a route to high dielectric constant materials with the inherent low loss of the base polymer," *J. Mater. Chem.*, vol. 21, no. 16, pp. 5897–5906, Apr. 2011, doi: 10.1039/c0jm04574h.

[15] A. Habib, N. Stelzer, and R. Haubner, "Fabrication of BaTiO3-PMMA Polymer Nanocomposite Thin / Thick Films and their Dielectric Properties," *Trans Tech PublA Habib, N Stelzer, R HaubnerSolid State Phenomena, 2009•Trans Tech Publ*, vol. 151, pp. 108–112, 2009, doi: 10.4028/WWW.SCIENTIFIC.NET/SSP.151.108.

[16] B. Xie *et al.*, "High Energy Storage Performance of PMMA Nanocomposites Utilizing Hierarchically Structured Nanowires Based on Interface Engineering," *ACS Appl. Mater. Interfaces*, vol. 13, no. 23, pp. 27382–27391, Jun. 2021, doi: 10.1021/acsami.1c03835.

[17] G. Zhang *et al.*, "Interfacial Polarization-Induced Loss Mechanisms in Polypropylene/BaTiO3 Nanocomposite Dielectrics," *Chem. Mater.*, vol. 28, no. 13, pp. 4646–4660, Jun. 2016, doi: 10.1021/acs.chemmater.6b01383.

[18] Z. Cai, X. Wang, B. Luo, W. Hong, L. Wu, and L. Li, "Dielectric response and breakdown behavior of polymer-ceramic nanocomposites: The effect of nanoparticle distribution," *Compos. Sci. Technol.*, vol. 145, pp. 105–113, 2017, doi: https://doi.org/10.1016/j.compscitech.2017.03.039.

[19] S. Dalle Vacche, Y. Leterrier, V. Michaud, D. Damjanovic, A. B. Aebersold, and J.-A. E. Månson, "Effect of interfacial interactions on the electromechanical response of

poly(vinylidene fluoride-trifluoroethylene)/BaTiO3 composites and its time dependence after poling," *Compos. Sci. Technol.*, vol. 114, pp. 103–109, 2015, doi: https://doi.org/10.1016/j.compscitech.2015.04.012.

[20] Q. M. Zhang, W. Cao, J. Zhao, and L. E. Cross, "Piezoelectric performance of piezoceramic-polymer composites with 2-2 connectivity-a combined theoretical and experimental study," *IEEE Trans. Ultrason. Ferroelectr. Freq. Control*, vol. 41, no. 4, pp. 556–564, 1994, doi: 10.1109/58.294118.

[21] M. Rani and U. Shanker, "Sun-light driven rapid photocatalytic degradation of methylene blue by poly(methyl methacrylate)/metal oxide nanocomposites," *Colloids Surfaces A Physicochem. Eng. Asp.*, vol. 559, pp. 136–147, 2018, doi: https://doi.org/10.1016/j.colsurfa.2018.09.040.

[22] A. Roy *et al.*, "Effects of interfacial interactions on structural, optical, thermal degradation properties and photocatalytic activity of low-density polyethylene/BaTiO3 nanocomposite," *Polymer (Guildf).*, vol. 276, p. 125932, 2023, doi: https://doi.org/10.1016/j.polymer.2023.125932.

[23] S. Atalay, E. Durmaz, and O. F. Seker, "Structural evolution and microwave absorption properties of $MnFe_2O_4$/$BaTiO_3$ nanoparticle systems and their composites," *J. Mater. Sci. Mater. Electron.*, vol. 37, no. 7, p. 488, 2026, doi: 10.1007/s10854-026-16924-7.

[24] G. Li, J. Xie, J. Wang, L. Xia, Y. Li, and W. Hu, "Nanoscale Surface Disorder for Enhanced Solar Absorption and Superior Visible-Light Photocatalytic Property in Ti-Rich BaTiO(3) Nanocrystals.," *ACS omega*, vol. 4, no. 6, pp. 9673–9679, Jun. 2019, doi: 10.1021/acsomega.9b00739.

[25] S. Requena, S. Lacoul, and Y. M. Strzhemechny, "Luminescent Properties of Surface Functionalized BaTiO3 Embedded in Poly(methyl methacrylate)," *Materials*, vol. 7, no. 1. pp. 471–483, 2014. doi: 10.3390/ma7010471.

[26] A. M. Bakr, A. Darwish, A. A. Azab, M. E. El Awady, A. A. Hamed, and A. Elzwawy, "Structural, dielectric, and antimicrobial evaluation of PMMA/CeO2 for optoelectronic devices," *Sci. Rep.*, vol. 14, no. 1, p. 2548, 2024, doi: 10.1038/s41598-024-52840-8.

[27] R. Ashiri, "Detailed FT-IR spectroscopy characterization and thermal analysis of synthesis of barium titanate nanoscale particles through a newly developed process," *Vib. Spectrosc.*, vol. 66, pp. 24–29, 2013, doi: https://doi.org/10.1016/j.vibspec.2013.02.001.

[28] S. N. Abed *et al.*, "Phytochemical Composition, Antibacterial, Antioxidant and Antidiabetic Potentials of Cydonia oblonga Bark," *Molecules*, vol. 27, no. 19. p. 6360, 2022. doi: 10.3390/molecules27196360.

[29] B. C. Smith, "Infrared Spectroscopy of Polymers X: Polyacrylates," *Spectroscopy*, 2023, [Online]. Available: https://api.semanticscholar.org/CorpusID:256495919

[30] S. A. Elsayed, M. A. Elhady, and A. K. Tammam, "Fabrication and Characterization of Sodium Carboxymethylcellulose Nanoparticles from Eichhornia crassipes Stem," *J. Polym. Environ.*, vol. 34, no. 5, p. 112, 2026, doi: 10.1007/s10924-026-03836-0.

[31] S. W. Lu, B. I. Lee, and L. A. Mann, "Carbonation of barium titanate powders studied by FT-IR technique," *Mater. Lett.*, vol. 43, no. 3, pp. 102–105, 2000, doi: https://doi.org/10.1016/S0167-577X(99)00253-0.

[32] S. W. Lu, B. I. Leea, and L. A. Mann, "Characterization of carbonate on BaTiO3 ceramic powders," *Mater. Res. Bull.*, vol. 35, no. 8, pp. 1303–1312, 2000, doi:

https://doi.org/10.1016/S0025-5408(00)00331-7.

[33] X. Zhu, D.-H. Lee, H. Chae, and S. M. Cho, "Abrupt change of luminescence spectrum in single-layer phosphorescent polymer light emitting diode," *J. Lumin.*, vol. 132, no. 1, pp. 12–15, 2012, doi: https://doi.org/10.1016/j.jlumin.2011.07.019.

[34] D. Hariharan *et al.*, "Enhanced photocatalysis and anticancer activity of green hydrothermal synthesized Ag@TiO2 nanoparticles," *J. Photochem. Photobiol. B Biol.*, vol. 202, p. 111636, 2020, doi: https://doi.org/10.1016/j.jphotobiol.2019.111636.

[35] V. Mishra *et al.*, "Electronic and optical properties of BaTiO3 across tetragonal to cubic phase transition: An experimental and theoretical investigation," *J. Appl. Phys.*, vol. 122, no. 6, p. 65105, Aug. 2017, doi: 10.1063/1.4997939.

[36] S. Chandrappa *et al.*, "Oxygen Vacancies and Ti3+ In-Gap Defects Dictate Photocatalytic H2 Generation in BaTiO3," *ACS Appl. Energy Mater.*, vol. 7, no. 23, pp. 11076–11085, Nov. 2024, doi: 10.1021/acsaem.4c02142.

[37] K. Wei *et al.*, "Photocatalytic properties of a new Z-scheme system BaTiO3/In2S3 with a core–shell structure," *RSC Adv.*, vol. 9, no. 20, pp. 11377–11384, Apr. 2019, doi: 10.1039/c8ra10592h.

[38] K. Karuppiah *et al.*, "Dye sensitized photocatalytic degradation of congo red and rhodamine B by 1,3,5-Benzenetricarboxylic acid based metal organic frameworks Ni3(BTC)2.12H2O, (Ni0.8Co0.2)3(BTC)2.12H2O and Cu3(BTC)2 under visible light," *Results Chem.*, vol. 14, p. 102099, 2025, doi: https://doi.org/10.1016/j.rechem.2025.102099.

[39] J. Feng *et al.*, "Fabrication of durable self-cleaning photocatalytic coating with long-term effective natural light photocatalytic degradation performance," *Chemosphere*, vol. 336, p. 139316, 2023, doi: https://doi.org/10.1016/j.chemosphere.2023.139316.

[40] M. A. Hoque and M. I. Guzman, "Photocatalytic Activity: Experimental Features to Report in Heterogeneous Photocatalysis," *Materials*, vol. 11, no. 10. p. 1990, 2018. doi: 10.3390/ma11101990.

[41] N. S. Alkayal, H. Altowairki, A. M. Alosaimi, and M. A. Hussein, "Network template-based cross-linked Poly(methyl methacrylate)/tin(IV) oxide nanocomposites for the photocatalytic degradation of MB under UV irradiation," *J. Mater. Res. Technol.*, vol. 18, pp. 2721–2734, 2022, doi: https://doi.org/10.1016/j.jmrt.2022.03.133.

[42] P. K. Singh *et al.*, "Enhanced pyroelectric and piezoelectric properties of PVDF – BaTiO3 nanocomposites layered samples," *Ferroelectrics*, vol. 551, no. 1, pp. 122–132, Oct. 2019, doi: 10.1080/00150193.2019.1658038.

[43] B. S. Athira *et al.*, "High-Performance Flexible Piezoelectric Nanogenerator Based on Electrospun PVDF-BaTiO3 Nanofibers for Self-Powered Vibration Sensing Applications," *ACS Appl. Mater. Interfaces*, vol. 14, no. 39, pp. 44239–44250, Sep. 2022, doi: 10.1021/acsami.2c07911.

[44] V. Fathollahzadeh and M. Khodaei, "Enhanced piezoelectric response of PVDF by incorporating of BaTiO3 nanoparticles and surface treatment," *J. Mater. Sci. Mater. Electron.*, vol. 35, no. 2, p. 107, 2024, doi: 10.1007/s10854-023-11848-y.

[45] Y. Wang, Y. Pu, and P. Zhang, "Investigation of dielectric relaxation in BaTiO3 ceramics modified with BiYO3 by impedance spectroscopy," *J. Alloys Compd.*, vol. 653, pp. 596–603, 2015, doi: https://doi.org/10.1016/j.jallcom.2015.09.012.

[46] Y. K. Vayunandana Reddy and D. Mergel, “Frequency and temperature-dependent dielectric properties of BaTiO3 thin film capacitors studied by complex impedance spectroscopy,” *Phys. B Condens. Matter*, vol. 391, no. 2, pp. 212–221, 2007, doi: https://doi.org/10.1016/j.physb.2006.09.021.

[47] T. J. Lewis, “Interfaces are the dominant feature of dielectrics at the nanometric level,” *IEEE Trans. Dielectr. Electr. Insul.*, vol. 11, no. 5, pp. 739–753, 2004, doi: 10.1109/TDEI.2004.1349779.

[48] K. Han *et al.*, “Suppression of energy dissipation and enhancement of breakdown strength in ferroelectric polymer–graphene percolative composites,” *J. Mater. Chem. C*, vol. 1, no. 42, pp. 7034–7042, Nov. 2013, doi: 10.1039/c3tc31556h.

[49] I. M. Ward, “Anelastic and dielectric effects in polymeric solids: N. G. McCrum, B. E. Read and G. Williams. Wiley: New York and London, 1967. 614in. by 912in. xv + 617 pp. 160s,” *Polymer (Guildf).*, vol. 9, p. 559, 1968, [Online]. Available: https://api.semanticscholar.org/CorpusID:136297685

[50] K. Zou *et al.*, “Flexible dielectric nanocomposites with simultaneously large discharge energy density and high energy efficiency utilizing (Pb,La)(Zr,Sn,Ti)O3 antiferroelectric nanoparticles as fillers,” *J. Mater. Chem. A*, vol. 7, no. 22, pp. 13473–13482, Jun. 2019, doi: 10.1039/c9ta01299k.

[51] K. Suematsu, M. Arimura, N. Uchiyama, and S. Saita, “Transparent BaTiO3/PMMA Nanocomposite Films for Display Technologies: Facile Surface Modification Approach for BaTiO3 Nanoparticles,” *ACS Appl. Nano Mater.*, vol. 1, no. 5, pp. 2430–2437, Apr. 2018, doi: 10.1021/acsanm.8b00650.

[52] A. K. Jonscher, “The ‘universal’ dielectric response,” *Nature*, vol. 267, no. 5613, pp. 673–679, 1977, doi: 10.1038/267673a0.

[53] G. Jian *et al.*, “Enhanced dielectric constant and energy density in a BaTiO3/polymer-matrix composite sponge,” *Commun. Mater.*, vol. 1, no. 1, p. 91, 2020, doi: 10.1038/s43246-020-00092-0.

[54] M. Belal Hossen and A. K. M. Akther Hossain, “Complex impedance and electric modulus studies of magnetic ceramic Ni0.27Cu0.10Zn0.63Fe2O4,” *J. Adv. Ceram.*, vol. 4, no. 3, pp. 217–225, 2015, doi: 10.1007/s40145-015-0152-2.

[55] J. T. S. Irvine, D. C. Sinclair, and A. R. West, “Electroceramics: Characterization by Impedance Spectroscopy,” *Adv. Mater.*, vol. 2, no. 3, pp. 132–138, 1990, doi: https://doi.org/10.1002/adma.19900020304.

[56] S. Boukheir *et al.*, “Electric Modulus Spectroscopic Studies of the Dielectric Properties of Carbon Nanotubes/Epoxy Polymer Composite Materials,” *J. Macromol. Sci. Part B*, vol. 57, no. 3, pp. 210–221, Mar. 2018, doi: 10.1080/00222348.2018.1439243.

[57] B. Behera, P. Nayak, and R. N. P. Choudhary, “Structural and electrical properties of KCa2Nb5O15 ceramics,” *Cent. Eur. J. Phys.*, vol. 6, no. 2, pp. 289–295, 2008, doi: 10.2478/s11534-008-0030-4.

[58] K. T. Selvi, K. A. Mangai, M. Priya, and S. Sagadevan, “Investigation of the dielectric and impedance properties of ZnO/MgO nanocomposite,” *Phys. B Condens. Matter*, vol. 594, p. 412355, 2020, doi: https://doi.org/10.1016/j.physb.2020.412355.

[59] T. S. Chanu, K. J. Singh, W. J. Singh, and K. N. Devi, “Dielectric Relaxation Behavior and Electrical Conduction Mechanism of PVA/ZnO Nanocomposites for Flexible Electronic

Device Application," *Phys. status solidi*, vol. 220, no. 21, p. 2300531, 2023, doi: https://doi.org/10.1002/pssa.202300531.

[60] S. K. Badge and A. V Deshpande, "Effect of vanadium doping on structural, dielectric and ferroelectric properties of bismuth titanate (Bi4Ti3O12) ceramics," *Ceram. Int.*, vol. 45, no. 12, pp. 15307–15313, 2019, doi: https://doi.org/10.1016/j.ceramint.2019.05.021.

[61] P Beena and HS Jayanna, "Dielectric studies and AC conductivity of piezoelectric barium titanate ceramic polymer composites," *Polym. Polym. Compos.*, vol. 27, no. 9, pp. 619–625, Nov. 2019, doi: 10.1177/0967391119856140.

[62] C. P. Charan and R. J. Sengwa, "P(VDF-HFP)/PMMA-BaTiO3 nanocomposite films of enhanced dielectric and optical properties through a fixed concentration of nanofiller and well tunable with polymer blend compositions," *J. Polym. Res.*, vol. 32, no. 11, p. 405, 2025, doi: 10.1007/s10965-025-04649-w.

[63] M. Hossain Khan;Sudipta Pal, "Frequency And Temperature Dependent Impedance Study In 50% BaTiO3- 50% La0.7Sr0.3MnO3 Nanocomposite," *Adv. Mater. Lett.*, vol. 5, no. 7, pp. 384–388, 2014, doi: 10.5185/amlett.2014.05552.

[64] A. Arya, M. Sadiq, and A. L. Sharma, "Effect of variation of different nanofillers on structural, electrical, dielectric, and transport properties of blend polymer nanocomposites," *Ionics (Kiel).*, vol. 24, no. 8, pp. 2295–2319, 2018, doi: 10.1007/s11581-017-2364-7.

[65] M. H. Khan, S. Pal, and E. Bose, "Frequency-dependent dielectric permittivity and electric modulus studies and an empirical scaling in (100−x)BaTiO3/(x)La0.7Ca0.3MnO3 composites," *Appl. Phys. A*, vol. 118, no. 3, pp. 907–912, 2015, doi: 10.1007/s00339-014-8810-8.